THE UNIVERSITY OF TOKYO

GRADUATE SCHOOL OF SCIENCES

Thesis

# TIME-INTEGRATED AND TIME-DEPENDENT DIRECTIONAL SEARCH FOR HIGH ENERGY ASTROPHYSICAL NEUTRINO POINT SOURCES IN SUPER-KAMIOKANDE

(スーパーカミオカンデにおける高エネルギー天体ニュートリノ点源の時間および方向の探索)

by

**XUBIN WANG**

Submitted in partial fulfillment of the

requirements for the degree of

Master of Science

2022

© Copyright by
XUBIN WANG
2022

## ACKNOWLEDGMENTS

I sincerely appreciate the support provided by Prof. Kimihiro Okumura in both study and life. His guidance which enlightens me through the whole research process is the indispensable key in completing this project. I am also truly grateful that he offered me the opportunity for such a research so that I did not get lost in this miserable time.

I also would like to express my appreciation to Dr. Mathieu Lamoureux, for the analysis libraries he has established for astrophysical neutrino field, and his patience answering to my questions. With his work and suggestions, I was able to carry on the research with less difficulties.

Prof. Katsuaki Asano has also gave me a lot of help in the past two years. As my mentor, he not only helped me in the life on campus, but also inspired me with his insightful understanding in the field of astrophysics.

Also I want to say thanks to Dr. Linyan Wan, as she answered the question about the UPMU sample which confused me for a long time.

Members in ICRR and Kamioka have provided me great help in getting used to the study of neutrino physics and life in Japan. I would especially thank Junjie Xia, Seungho Han from RCCN and Jiahui Feng from Kyoto University.

And my sincere thank give to all members in SK group, for none of the analysis work could be done without the the experiment setup and software development.

Last but not least, thank you my parents, my family, and my friends. Without your support, I would never be able to make this far.

# TIME-INTEGRATED AND TIME-DEPENDENT DIRECTIONAL SEARCH FOR HIGH ENERGY ASTROPHYSICAL NEUTRINO POINT SOURCES IN SUPER-KAMIOKANDE

(スーパーカミオカンデにおける高エネルギー天体ニュートリノ点源の時間および方向の探索)

**XUBIN WANG**

ABSTRACT

Astrophysical high-energy neutrino point sources has been considered of extreme interest in the field of both astrophysics and particle physics. The mysterious neutral lepton with supper tiny mass, effected by neither the magnetic field nor the cosmic microwave background, is believed to be able to carry the information of the ultra-high-energy celestial objects and phenomena, and even the cosmic accelerator that has confused scientists for a long time. Very few is known to us about the astrophysical neutrinos or their sources up until now, but the effort has never been stopped and remarkable progress has been achieved.

Using the data collected by the water Cherenkov detector Super-Kamiokande during 2008 and 2018, we performed both a time-integrated and a time-dependent search for the potential candidates of the high-energy astrophysical neutrino sources with upward-going muon events via unbinned maximum likelihood method. No excess with respect to the background is found in either search.

The most probable location to have a point source in the full sky is found at (198.3°, 15.1°) in J2000 equatorial coordinate system with pre-trial $p$-value of $1.18 \times 10^{-4}$ and post-trial $p$-value of 79.2% in the time-integrated search. The upper limits

of the neutrino fluence and flux are set to $\Phi = 2.06 \times 10^2$ [GeVcm$^{-2}$] and $\varphi^{upper} = 4.53 \times 10^{-7}$ cm$^{-2}$s$^{-1}$, respectively.

In the time-dependent search, the most significant cluster is at $(118.0^\circ, -62.7^\circ)$ on 2010.10.27 13:09:42 JST and half emission duration $\hat{\sigma}_t = 9.25 \times 10^3$ s. The pre-trial $p$-value is $2.24 \times 10^{-4}$ and post-trial $p$-value is 33.4%. Neutrino fluence upper limit is $\Phi = 7.86 \times 10^1$ GeVcm$^{-2}$, with the emission time interval estimated by $1.85 \times 10^4$ s $(2\hat{\sigma}_t)$.

The algorithm and the library of the numerical analysis established in this study can be applied on future relative researches on topics regarding the astrophysical neutrinos.

## CONTENTS

## LIST OF TABLES

## LIST OF FIGURES

# CHAPTER 1

# Introduction

## 1.1 NEUTRINO

In 1930, Pauli first postulated the existence of neutrinos to explain the momentum conservation of beta decay. The electron anti neutrino was first observed by Reines and Cowan in 1956 at a nuclear reactor. Using the neutrino beam produced by the decay of charged pions, the existence of the muon-neutrino was confirmed by Danby in 1962. The third kind of neutrino, tau-neutrino, was discovered by Direct Observation of the Nu Tau (DONuT) Experiment in 2001.

In the standard model, neutrinos were first thought to be massless, neutral leptons. Although they have been proved to have mass now, it is negligible when considering the effect of gravity. As a result, the only interaction channel for them is weak interaction. The neutrinos detected on Earth are mainly generated via nuclear reactions in the core of the sun and high energy cosmic rays interacting with nucleus in the atmosphere. Except for natural sources, nuclear reactors and accelerators can also generate neutrinos and are widely used in the studies of neutrino properties.

The discovery of neutrino oscillation can date back to the Homestake Experiment in 1960s, which observed a huge difference between the measured electron-neutrino flux and the one predicted by the standard solar model. This solar neutrino problem had remained unsolved for about thirty years before physicists realized that the properties of neutrino that had been assumed might not be accurate. If the three kinds of neutrinos are massive and have mass differences, their flavor eigenstates will be different from their mass eigenstates, and thus the flavor can oscillate to one that differs from what the neutrino is generated with. Such a phenomenon is called neu-

trino oscillation. In 1998, Super-Kamiokande Experiment (SK) found the evidence of neutrino oscillation via the asymmetry between the upward-going and downward-going atmospheric neutrino. Then with the measurement of solar neutrinos at SK and Sudbury Neutrino Observatory, solar neutrino problem was well explained.

The first observation of astrophysical neutrinos outside solar system was on February 23rd, 1987, from a supernova explosion in Large Magellanic Cloud 51.4kpc away from the Earth. This supernova was numbered as SN1987A, and SK, Irvine-Michigan-Brookhaven Experiment (IMB) and Baksan Underground Scintillation Telescope (BUST) detected 11, 8 and 5 neutrinos, respectively. In the supernova model, 99% of the energy of the core collapse supernova will be released via neutrino emission. This observation not only examined the model, but also remarked the beginning of using neutrino as a tool to study astronomy.

## 1.2 HIGH-ENERGY ASTROPHYSICAL NEUTRINOS

### 1.2.1 Overview

High-energy astrophysical neutrinos refer to the neutrinos from galactic or extra-galactic distant objects with energy above 1 GeV. Unlike solar neutrinos or supernova neutrinos, high-energy neutrinos are not produced directly by the celestial bodies. Instead, they are produced as a result of the cosmic accelerator, which is a kind of electromagnetic accelerator. More details will be discussed in 1.2.2.

Protons accelerated by the cosmic accelerator can scatter off another accelerated proton or a photon and produce mesons through the following channel:

$$p + \gamma \rightarrow \pi^+ + n \tag{1.1}$$

$$p + \gamma \rightarrow \pi^0 + p \tag{1.2}$$

$$p + p \rightarrow \pi^{\pm}, \pi^{0} \tag{1.3}$$

The charged and neutral pions, together with protons and neutrons, can undergo the following decays:

$$\pi^{+} \rightarrow \mu^{+}\nu_{\mu} \rightarrow e^{+} + \nu_{e} + \bar{\nu}_{\mu} + \nu_{\mu} \tag{1.4}$$

$$\pi^{0} \rightarrow 2\gamma \tag{1.5}$$

Among the produced particles, photons, neutrinos and neutrons are neutral and will escape from accelerator. Additionally, the neutron can decay into a proton:

$$n \rightarrow p + e^{-} + \bar{\nu_{e}} \tag{1.6}$$

Energy distribution of neutrinos generated in this way will follow a power spectrum. This will be introduced in details in Section 1.4.1.

Although cosmic rays (mainly consists of protons), gamma rays and neutrinos are all produced in this process, neutrino has advantages compared with the other two. First, it is electromagnetic neutral, meaning that it will not be deflected by the magnetic field existing in the galaxy and so that the direction information of the source is not lost. Second, its cross section is extremely small so that the probability that it scatters off another particle is tiny. Gamma rays can be blocked by the opaque objects, and cosmic rays will interact with the cosmic microwave background (CMB) at high-energy region.

### 1.2.2 Cosmic Accelerator

The cosmic rays we have observed on Earth have energies that is much higher than the expected thermal energies of cosmic rays emitted by astrophysical objects. The most commonly accepted explanation of such a phenomenon is that the cosmic rays are accelerated by the electromagnetic fields known as the cosmic accelerator. Although many models have been established, the mechanism of acceleration still remains unknown to us.

The mechanisms of acceleration can be different for different astrophysical objects, and the process may consist of more than one mechanism. Among the mechanisms, shock acceleration is widely included in the scenarios of many astrophysical objects[34]. In this model, the accelerating region contains two parts: upstream and downstream. The upstream is a region full of charged particles with high velocity (mainly protons) generated by some certain kind of driven force such as the supernova explosion. In the downstream, on the other hand, the velocity of the charged particle is smaller. The boundary between the upstream and downstream is called the shock front. When a charged particle moves across the shock front, it can scatter on a magnetic irregularity and change the momentum direction. Then it will move across the shock front and scatter again. In the process of bouncing back and forth, the energy of the particle will increase or decrease, depending on the scattering angles, but in average the particle gains energy. After the energy of the particle is large enough, it has the probability to escape from the shock.

Such kind of acceleration can take place both galactically and extra-galactically. There is an energy limit which the particle trapped within the magnetic field in the galaxy can reach. As a result, the cosmic rays with the highest energies are probably generated from extra-galactical sources.

## 1.3 POTENTIAL NEUTRINO SOURCE CANDIDATES

Except for solar neutrinos and supernova neutrinos, no astrophysical neutrino event had been observed before 2017. However, on 22 September 2017, IceCube detected an ultra-high-energy neutrino event of approximately 290 TeV, labeled as IceCube-170922A. Following this observation, IceCube performed a search for neutrino point sources at the position of TXS 0506+056, but independent of IceCube-170922A[30]. In that search, they used the time-dependent search method which is similar to what is used in this study, and discovered an excess of neutrino emission of a confidential level above $3\sigma$ between 2014 and 2015 (Figure 1.1). This provided a strong evidence that blazars could be the sources of high-energy astrophysical neutrinos.

There are, however, many potential neutrino source candidates that are considered to generate neutrinos theoretically. In this part I will briefly introduce some of them.

### 1.3.1 Active Galactic Nucleus

An Active Galactic Nucleus (AGN) is super massive black hole (BH) with an accretion disk located at the center of a distant galaxy.

The BH and accretion disk is surrounded by clouds of gas moving rapidly in the potential of the BH and a torus or warped disk of gas and dust well outside the accretion disk. Relativistic collimated jets are emitted perpendicular to the disk. Figure 1.2 shows a schematic of AGN. Those AGN with the jet direction pointing to the observer are called the blazar[59].

When matter in the accretion disk fall into the BH, it creates an accretion shock, leading to the first order Fermi acceleration of charged particles including protons. These ultrarelativistic protons can collide with intensive photon fields and produce high-energy neutrinos[57].

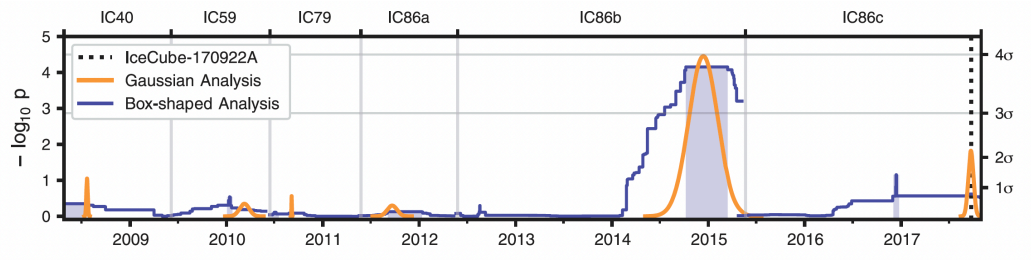


**(a)**

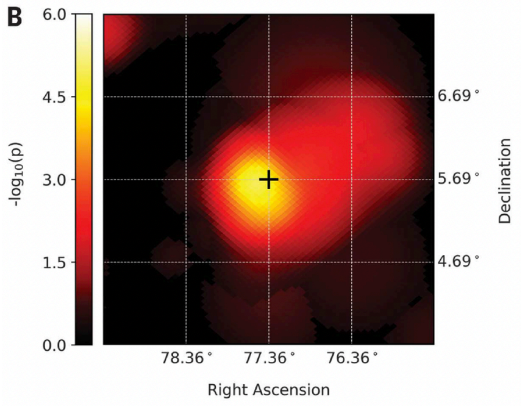


**(b)**

**Figure 1.1:** Top: Results of time-dependent analysis. Black dashed line represents IceCube-170922A. A significant peak over $3\sigma$ was discovered during IC86b, at around the beginning of 2015. Bottom: Skymap of $p$-value. Black cross at the middle is TXS 0506+056. Figures are taken from [30].

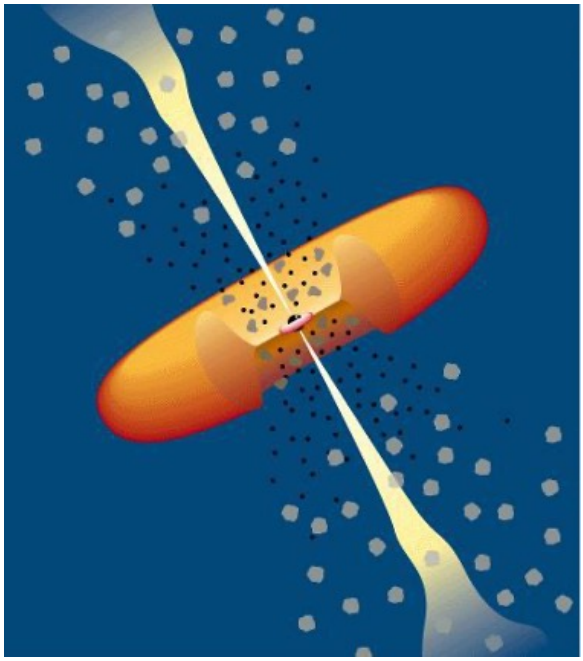

**Figure 1.2:** Schematic of radio-loud AGN[59]

### 1.3.2 Gamma-Ray Burst

Gamma-ray burst (GRB) are extremely luminous electromagnetic radiation events observed in distant galaxies.

The GRB is considered to be produced by the dissipation of an expanding fireball. The ultrarelativistic particles in the fireball are generated in the collapse of a massive rotating star core or the merger of a neutron star with another neutron star or blackhole, where large amount of gravitational energy is released in a short time in a small region[49].

In this fireball model, protons can undergo Fermi acceleration to energies up to $10^20$ eV[61]. Then high-energy neutrinos can be generated through the photomeson production.

### 1.3.3 Supernova Remnant

Supernova Remnants (SNR) are expanding materials ejected from supernovae explosions bounded by shock waves. Figure 1.3 is one of the most famous supernova remnant, Crab Nebula, which is also a plerion (pulsar wind nebula).

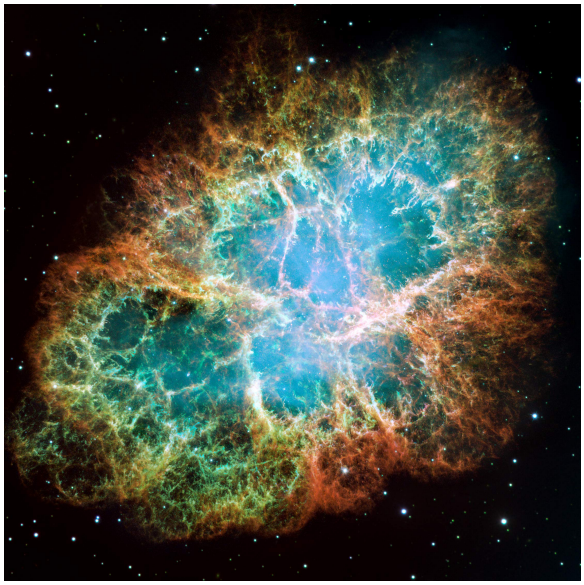

**Figure 1.3:** Crab Nebula[51]

The possible acceleration mechanism SNR have is the diffusive shock acceleration[33]. When the ejecta meets the surrounding interstellar medium, it is possible to produce neutrinos via pion production.

### 1.3.4 Magnetar

Magnetars are rotating neutron stars with strong magnetic fields ($\sim 10^{15}G$).

There are two main energy source to power the magnetars: the magnetic power and the spin-down power[28]. For magnetars whose spin and magnetic momentum are in opposite directions, spin-induced electric fields can accelerate the protons from surfaces. Then they will scatter off the photons generated in the decay of strong

magnetic fields and produce pions, which will later decay into neutrinos.

The particles emitted by magnetars are not isotropic but will concentrate in a certain direction. The expected neutrino flux will be magnificent in that direction, yet much lower in others. It is not very likely the direction happens to point at Earth. However, if it does, it will be helpful for the study on astrophysical neutrinos and magnetar structure.

## 1.4 MULTI-MESSENGER ASTRONOMY

After the detection of high-energy neutrino event IceCube-170922A in 2017, IceCube sent out an alert to all gamma ray observatories. It was later found out that the blazar TXS 0506+56, whose position is coincident with the direction of the neutrino event, was in a flaring state. From that time, a series of gamma-ray observation in a various of wavelength range followed, and high-energy gamma rays were confirmed to be detected from that blazar (Figure 1.4)[31].

This kind of research, usually called multi-messenger research, has been proved very useful, as various messengers can carry information of different process. Other than neutrinos, cosmic rays, electromagnetic radiation and gravitational wave are also the major messengers used in astronomy studies.

### 1.4.1 Cosmic Rays

Cosmic rays (CR) are high energy astrophysical particles mainly consist of protons (90%), nucleus (9%) and electrons (1%)[53]. I have briefly introduced their origins and the acceleration mechanism in previous chapters so I will mainly introduce their energy spectrum in this chapter.

Energy distribution of cosmic rays follows a power spectrum, with a spectral index

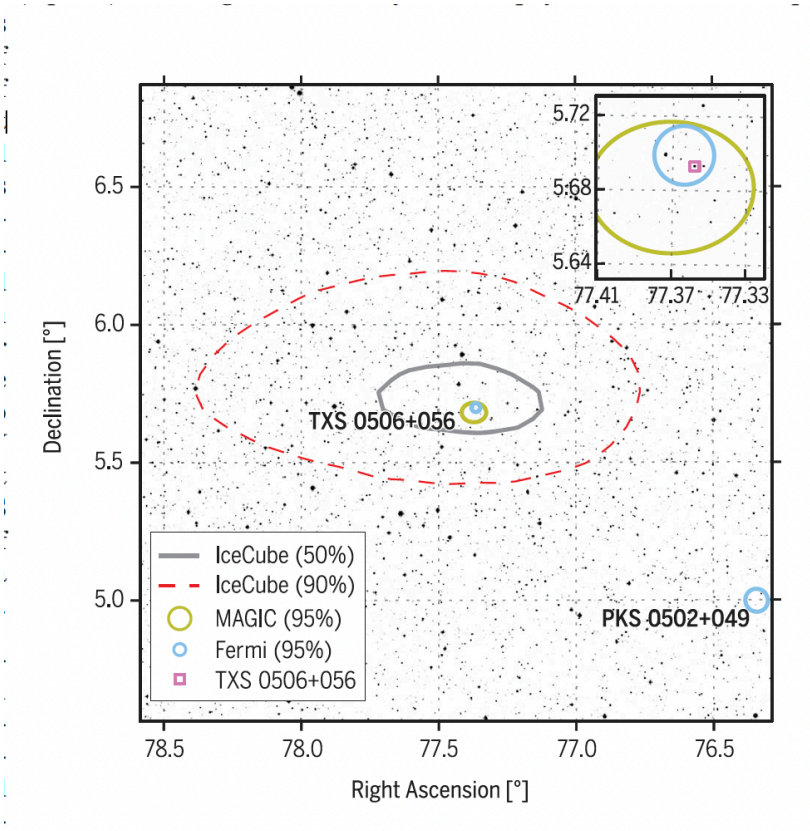


**Figure 1.4:** Multimessenger observation of TXS 0506+056 via neutrino and gamma rays by IceCube, MAGIC and Fermi. Figure taken from [31]

gamma, shown in Figure 1.5. There are two important structures: a knee, and an ankle. The knee is at $\sim 10^15eV$. Below the knee, gamma  2.7. The ankle is at $\sim 10^19eV$. Above that gamma  2.6. Between the knee and the ankle, gamma  3.1.

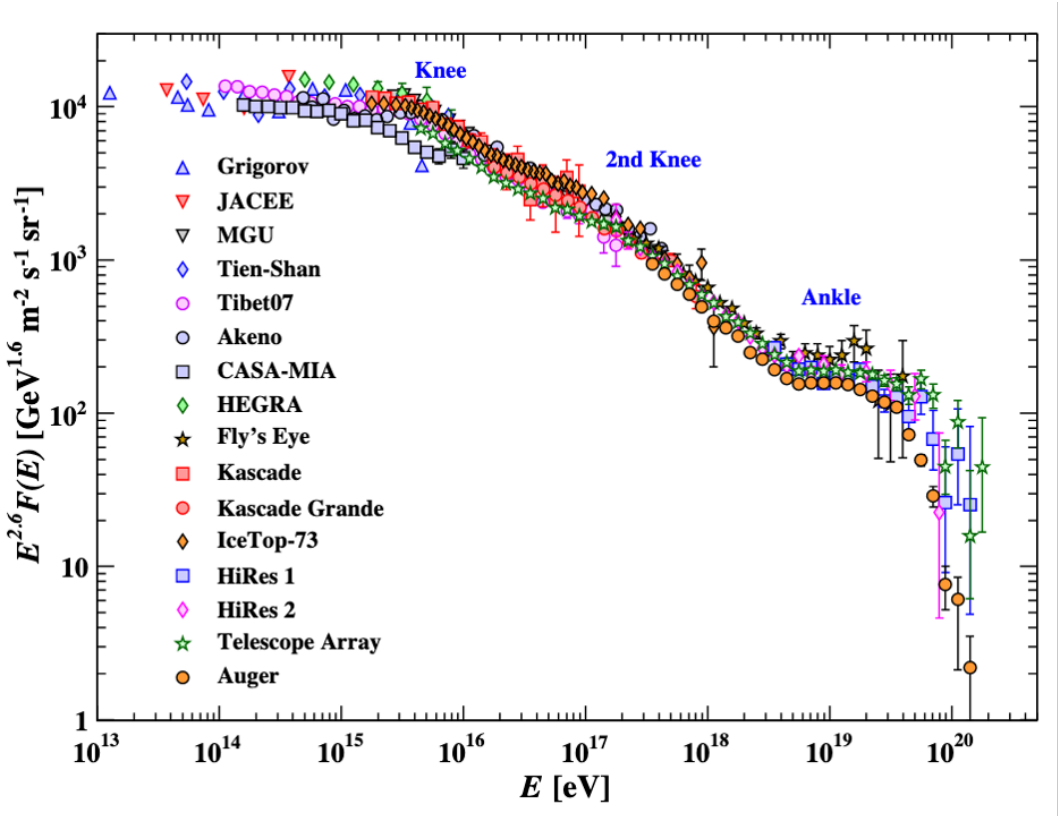


**Figure 1.5:** Energy spectrum of CR [38]

The spectrum does not continue to infinity. At around $5 \times 10^{19}$, there is a rapid steepening in the spectrum called the Greisen-Zatsepin-Kuzmin (GZK) cutoff[37, 63]. Protons with energies higher than this threshold undergo inelastic interactions with CMB:

$$p + \gamma \rightarrow \pi^0 + p \tag{1.7}$$

### 1.4.2 Gamma rays

Gamma rays can be generated both leptonically and hadronically.

Leptonic process refers to the synchrotron radiation of accelerated electrons propagating in strong magnetic fields. Since the synchrotron radiation will be suppressed for particles with larger mass, heavier particles like protons does not have much contribution to this process.

The hadronic process is similar to neutrino creation, with only charged pion decay being changed to neutral pion decay. Since neutrinos and gamma rays are produced at the same time, and neither of them are deflected by the magnetic fields in the galaxy, they can be used as the triggers of each other.

### 1.4.3 Gravitational Waves

Gravitational wave (GW) is a different kind of messenger in comparison with CR, gamma rays and neutrinos. It is not particle, but the propagation of the change in curvature of spacetime. On August 17th, 2017, LIGO and Virgo collaboration observed the first evidence of gravitational wave. This not only proved the general relativistic, but also provided a new way and aspect to study the astrophysics and cosmology.

GWs are usually generated by the merger of two massive objects, such as neutron star and neutron star, black hole and black hole, and neutron star and black hole. After the merging, a magnificent amount of energy is released in the form of GW. GW travels in the universe with the speed of light. Its direction does not change and hardly lose any energy through its propagation, making it an extremely useful messenger.

Current observatories of GW including LIGO, Virgo and KAGRA. Each of the can detect the GW signal from all directions. After a signal is received, an alert is sent to all the astronomical observatories all over the world and following observation

of other messengers can be carried out immediately.

## 1.5 PREVIOUS RELATED SEARCH

- SKI-III:

  In 2009, a time-integrated search on data from SKI to SKIII was conducted[58]. Only up-going muon sample was used. Sensitivity in this research is estimated to $3 \times 10^{-7}$ $\mathrm{cm}^{-2}\mathrm{s}^{-1}$ in the region of declination of $(-30°, 0°)$. The lowest neutrino flux limit averaged in right ascension is set to $6 \times 10^{-8}$ $\mathrm{cm}^{-2}\mathrm{s}^{-1}$ at around dec$= -54°$.

- IceCube:

  IceCube searched for the time and space clustering of high-energy neutrinos time-dependently in 2020 using data from 2012 to 2017, and in 2015 using data from 2008 to 2012[5, 4].

- ANTARES:

  ANTARES searched for point-like neutrino sources time-integrally with 9-year data and 11-year data in 2017 and 2020, respectively.[21, 43]

# CHAPTER 2

## Super-Kamiokande

### 2.1 OVERVIEW

Super-Kamiokande (SK) is a water Cherenkov detector. The detector lies 1,000 meters under Mt. Ikenoyama, Hida City, Gifu Prefecture, Japan. The main part of the detector is a stainless steel cylindrical water tank with a diameter of 39 meters and height of 42 meters. This water tank contains 50,000 tons of ultra pure water. On the wall of the tank and outside of the tank, there are in total 13,000 photomultipliers (PMT). The rock above and around the detector create a good shelter which shields most of the cosmic rays of energies below 1.3 TeV, and only about $1 \times 10^{-5}$ of the cosmic muons arrive at the earth surface can reach the detector. Figure 2.1 is a schematic of SK.

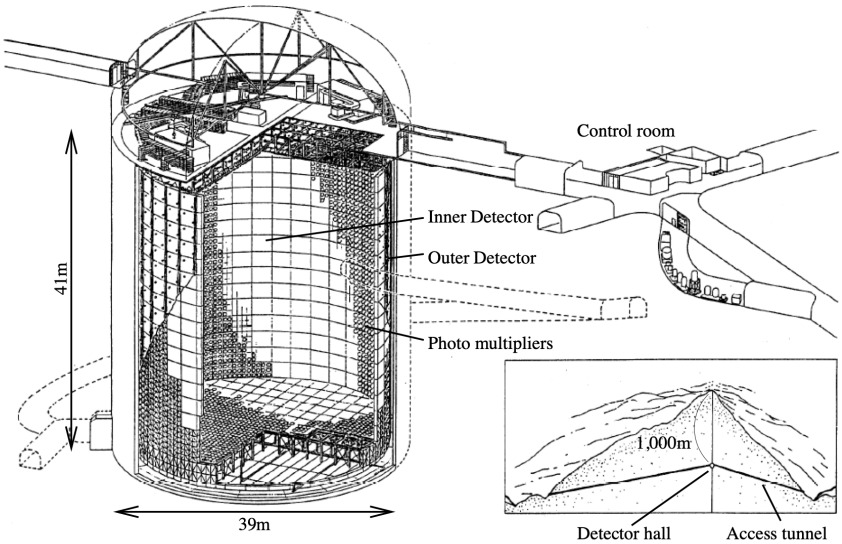


**Figure 2.1:** A schematic of SK.[44]

The SK detector contains two parts: the inner detector (ID) and outer detector

(OD). ID uses about 11,000 20-inch PMTs located 2.6 meters inward from the wall of the tank. OD is placed 2.2 meters from the wall and 2.1 meters from the top and bottom of the tank, consisting of 1,885 8-inch PMTs. The OD wall is covered with white Tyvek sheet to maximize light detection efficiency. Additionally 26 sets of vertical and horizontal Helmholtz coils are lined up along the wall, reducing the geomagnetic field inside the tank from 450 mG to 50 mG. The frame structure is shown in Figure 2.2.

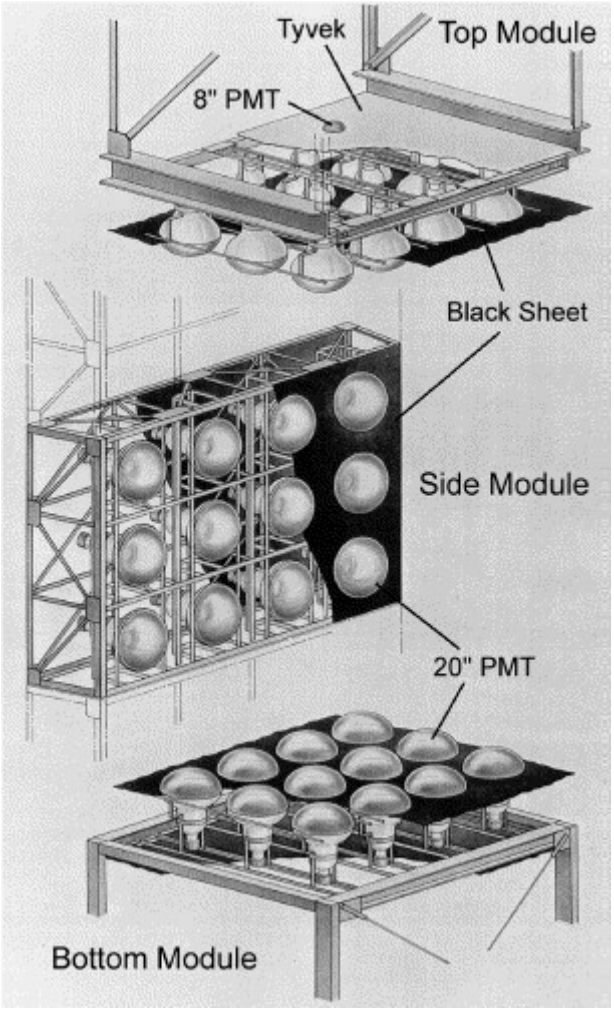


**Figure 2.2:** Frame structure which supports PMTs.[35]

SK started to operate since 1 April 1996, and has 6 completed phases (from SK-I

to SK-VI). During SK-II in 2001, more than half of the PMTs were destroyed due to an implosion of one bottom PMT, causing the ID photon coverage rate dropping to 19%. In 2008, front-end electronics were upgraded. From SK-VI, gadolinium (Gd) was dissolved in the ultra-pure water to make it easier to separate neutrinos from antineutrinos. The latest phase SK-VII started from 1 June 2022. In this phase the Gd concentration will be increased from 0.01% to 0.03%.

## 2.2 CHERENKOV RADIATION

SK detect charged particles via the emitted Cherenkov lights that hit the PMTs. The speed of light in dielectrics is smaller than that in the vacuum, making it possible for ultra-relativistic charged particle to move with a velocity larger than that. When such a situation occurs, an electromagnetic shock called the Cherenkov radiation is created. Using the Huygens-Fresnel principle, it is predicted that the emitted lights form a cone centered at the particle traveling direction with an opening angle related to the velocity of the particle:

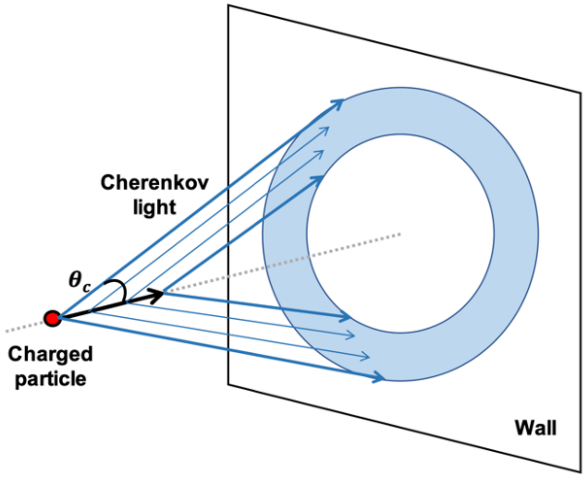


**Figure 2.3:** Cherenkov radiation light cone.[9]

$$\cos\theta_c = \frac{1}{n\beta} \tag{2.1}$$

Here $\theta_c$ is the opening angle, $n$ is the refractive index of the dielectric, and $\beta = v/c$. The number of photons emitted per unit traveling length per unit wave length as a function of wave length and $\beta$ can be given by

$$\frac{d^2N}{dxd\lambda} = \frac{2\pi\alpha}{\lambda^2}\left(1 - \frac{1}{\beta^2 n^2}\right) \tag{2.2}$$

where $\alpha$ is the fine structure constant. The $\beta$ threshold of Cherenkov radiation then can be obtained as

$$\beta_{thr} = \frac{1}{n} \tag{2.3}$$

and using this the momentum and energy threshold is given by

$$p_{thr} = \frac{mc}{\sqrt{n^2 - 1}} \tag{2.4}$$

$$E_{thr} = \frac{mc^2 n}{\sqrt{n^2 - 1}} \tag{2.5}$$

In Table 2.1 thresholds for different particles in water are listed. PMTs in SK are sensitive to light with wave lengths from 340 nm to 600 nm, and the spectrum in this region of water is shown in Figure 2.4.

## 2.3 PHOTOMULTIPLIER

Two types of PMT are installed in SK: 8-inch PMT for OD and 20-inch PMT for ID.

The ID PMT is Hamamatsu R3600 PMT developed by Hamamatsu Photonics K.K., and the structure is shown in Figure 2.5. The photocathodes are made of

**Table 2.1:** Cherenkov energy thresholds in water for different particles.

| Particle | Rest Mass [MeV] | Threshold [MeV] |
|---|---|---|
| $e^{\pm}$ | 0.511 | 0.775 |
| $\mu^{\pm}$ | 105.7 | 160.3 |
| $\pi^{\pm}$ | 139.6 | 211.7 |
| $K^{\pm}$ | 493.7 | 748.8 |
| $p$ | 938.3 | 1408.9 |

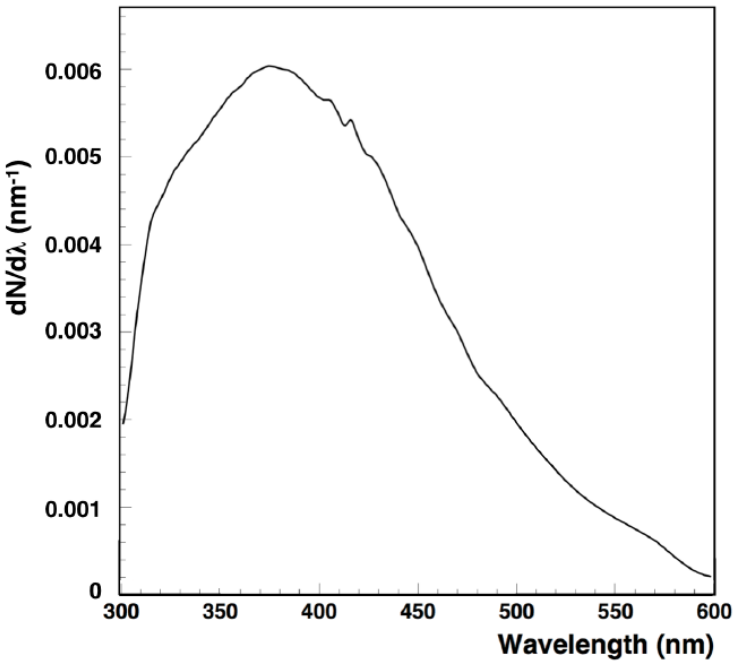


**Figure 2.4:** Spectrum of Cherenkov radiation in water.[48]

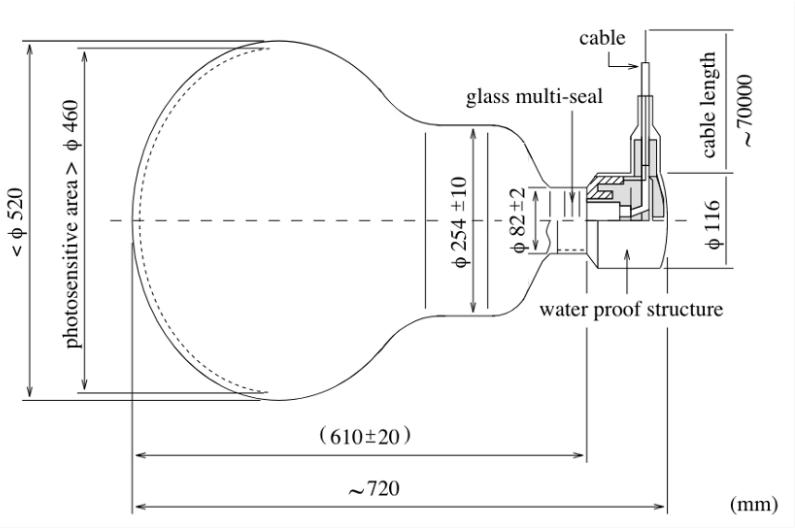


**Figure 2.5:** 20-inch PMT.[35]

Bialkali (Sb-K-Cs). The quantum efficiency peaks at around 360 nm to 400 nm to a value of 22% as shown in Figure 2.6.

The OD PMT has been used in SK since the accident in 2001 is Hamamatsu R5912 PMT. Each PMT is attached to a 60cm × 60cm × 1.3cm wavelength-shifting (WS) plate made of acrylic-doped panels to absorb ultraviolet and emit blue green light which is closer to the sensitivity peak of the PMT.

Every PMT has been covered by a 12 mm ultraviolet transparent acrylic dome and a fiberglass reinforced plastic (FRP) case to prevent chain explosion in SK-II (Figure 2.7).

## 2.4 ELECTRONICS AND DATA ACQUISITION SYSTEM

Since SK-IV, the front-end electronics used for data acquisition (DAQ) system is charge-to-time converter (QTC) based electronics with ethernet (QBEE)[52].

Each QBEE board consists of 8 QTCs, and each QTC connects to 3 PMTs. Charge signal from PMT is first integrated by QTC, and then the output signal is

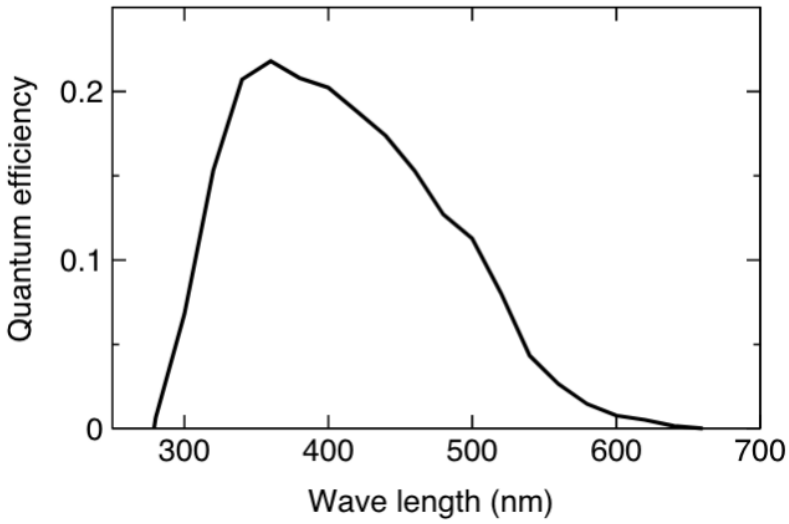


**Figure 2.6:** 20-inch PMT quantum efficiency distribution as a function of wavelength.[32]

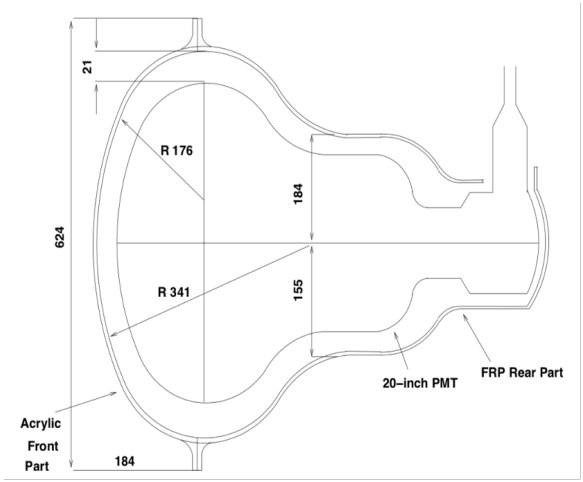


**Figure 2.7:** FRP case and acrylic cover for ID PMT.[35]

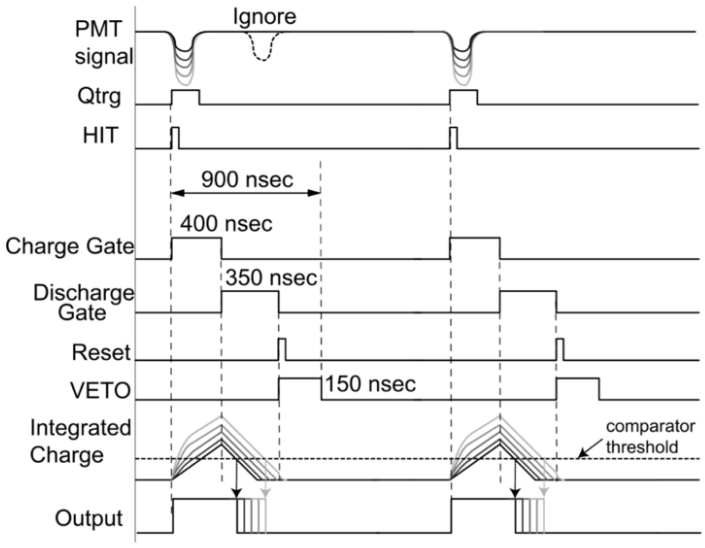


**Figure 2.8:** Timing chart of QTC in QBEE.[52]

sent to time-to-digital converter (TDC). The digital signal is then recorded by a field-programmable gate array (FPGA) at 60 kHz for data-sort mapping (DSM) (Figure 2.8). Four DSM chips are installed in each QBEE, and their outputs are sent to the system-interface controler (SIC) which sorts the data and stores them into first-in first-out (FIFO) memory (Figure 2.9).

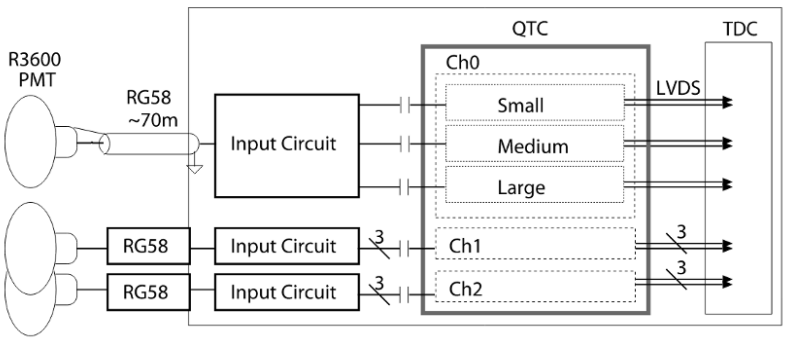


**Figure 2.9:** Block diagram of the QTC.[52]

One QBEE has the dynamic charge range from 0.2 to 2,500 pC, and there are three gains, 1, 1/7, 1/49, corresponding to small, medium, large, in each QTC channel.

Trigger used before SK-IV is the hardware trigger. Together with the upgrade in 2008, the hardware trigger was replaced with software trigger, allowing the event width to change according to the trigger type. The triggers include super low energy (SLE), low energy (LE), high energy (HE), special high energy (SHE), outer detector (OD) triggers, and after trigger (AFT). AFT is used for the neutron tagging system.

## 2.5 WATER AND AIR SYSTEM

The water used in SK is the underground water from the mine. The dust in the water can scatter or absorb the light and cause the detector sensitivity to decrease. The water may also be contaminated by the radioactive materials from the rock such as the radon and radium. These radioactive materials increase noise hits and is the main background in low-energy neutrino measurements. The water purification system is applied in SK for those reasons mentioned above. About 50 tons of water are circulated and purified in this system per hour. Additionally a heat exchange system is installed to keep the water temperature at 13.6 degrees.

The air is also purified by an air purification system which pumps radon-free air into the tank to prevent the radioactive materials being dissolved in the water.

# CHAPTER 3

# Upward-Going Muon

## 3.1 SK DATA SAMPLE

The events SK collected are classified into three types: fully contained (FC), partially contained (PC) and upward-going muon (UPMU). UPMU are additionally classified as stopping, through-going and showering. Figure 3.1 shows the schematic of different types of samples. For FC and PC, neutrinos interact with the water and create secondary particles within the ID volume. The difference is that all charged particles stop within the ID volume for FC, and at least one particle exits the ID volume and deposit energy in OD for PC. For UPMU, the muon neutrinos interact with the rock around the detector and create energetic muons that enters the detector from directions below horizon. If the muon stops and decays inside the detector, it is classified as stopping muon. Both through-going and showering muons pass through the detector, but showering muons pass the shower selection.

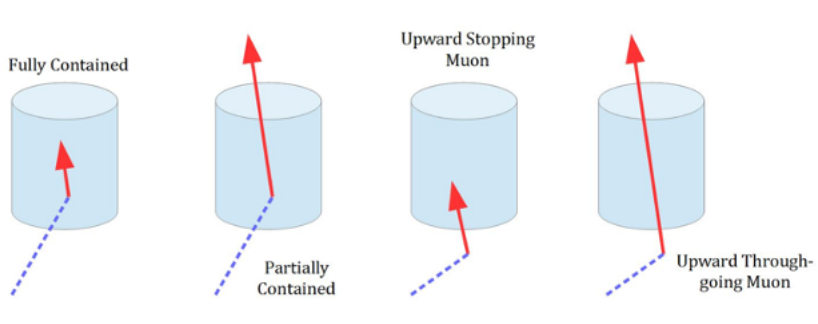


**Figure 3.1:** Schematic of SK samples.[62]

FC, PC and UPMU have mean energies of 1 GeV, 10 GeV, and 10 to 100 GeV respectively. The simulated neutrino energy distribution is shown in Figure 3.2.

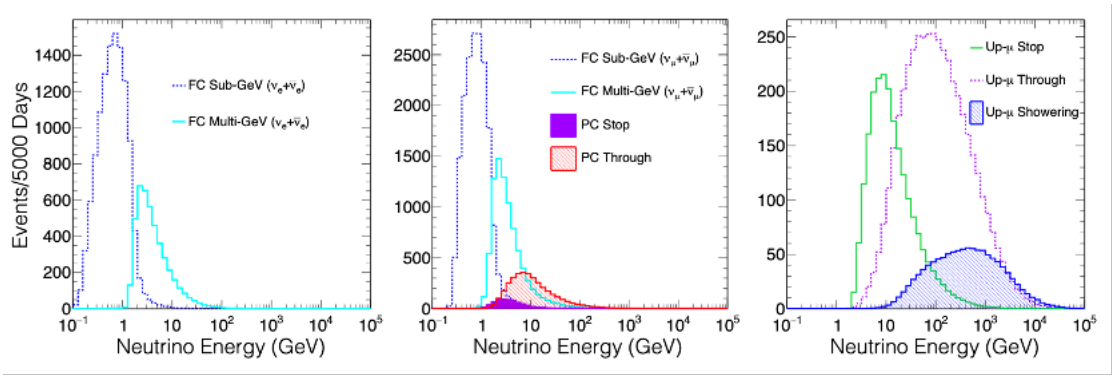


**Figure 3.2:** Expected atmospheric neutrino energy distribution for different samples.[8]

## 3.2 DATA REDUCTION

SK receives a huge amount of events at the trigger level, yet only a tiny percent of them are the true signal events. The major parts of the background here is the CR muons and PMT noises. In order to reject the background events and classify the signal events, data reduction is of vital importance. Here I will briefly introduce the major steps of UPMU reduction. More details for UPMU and FC, PC can be found in [25].

In the first reduction, a charge cut which requires

$$6,000 \text{ p.e.} \leq \text{PE}_{300} < 1,750,000 \text{ p.e.} \tag{3.1}$$

is applied. Here $\text{PE}_{300}$ is the total number of observed photoelectrons (p.e.) within 300 ns. This eliminate the low energy and extremely high energy events. The requirement for the track length of UPMU is longer than 7 m, and a muon with a momentum of 1 GeV and a track length of 3.5 m produces 6,000 p.e.. If the ID charge is larger than 1,750,000 p.e., the muon fitters will fail because the electronics become saturated.

The second reduction downward-going muons are rejected, for they are mostly

CR muons. To do so, a logic tree of 7 different muon fitters specialized to fit stopping muons, through-going muons and muons with bremstrahlung are involved. For one fitter, those events classified as upward with a goodness-of-fit larger than the threshold are accepted, and those classified as downward with a goodness-of-fit larger than the threshold are rejected. If the event is classified as horizontal with a goodness-of-fit above the threshold or all of the goodness-of-fits are below the thresholds, the event will be passed to the next fitter and repeat the steps above. If none of the fitters classify the event as upward or downward with a goodness-of-fit larger than the threshold, but at least one of them classified it as horizontal with a goodness-of-fit above the threshold, it will be accepted. Otherwise, it is rejected.

The third reduction is eye-scanning. And eventually the final reduction classifies the events. To classify whether an event is a stopping or through-going (including showering) muon, a criteria is used to determine the entry or exit. If the number of OD hits within 800 ns and with 8 m from the entry or exit projected by the track is greater than 10, then this entry or exit is considered to be an entry or exit signal. If both entry and exit signal exist, and the distance between the entry and exit is greater than 7 m, the event is classified as a through-going muon. If only entry signal exists and the fitted momentum using Cherenkov light is not less than 1.6 GeV, corresponding to 7 m track length, it is classified as a stopping muon. For the showering muons, an extra chi-squared test based on the observed charge and the expected charge of non-showering muon is applied. Events pass all selections will be reconstructed.

## 3.3 EVENT RECONSTRUCTION

Information including energy, time, direction and neutrino type can be reconstructed using the time, charge and position of PMTs. The current fitting algorithm used by SK is called APFit. I will only cover the reconstruction procedure of UPMU reconstruction, which is same to part of the single-ring FC and PC reconstruction. [25] introduces the reconstruction for all situations.

First part is the vertex fitting. This is done using the time information of hit PMTs.

The first step is the point fit. In this step, it is assumed that all photons from the Cherenkov radiation are emitted at the same time from one point. The goodness of the fit is dined as:

$$G(t_0) = \frac{1}{N}\sum_i \exp\left(-\frac{(t_i - t_0)^2}{2(1.5\sigma)^2}\right) \tag{3.2}$$

where $t_i$ is the time residual equals to the photon arrive time minus time of fly of the photon for the $i^{th}$ PMT, $t_0$ is a free parameter to be fitted to maximize $G(t_0)$ and $\sigma = 2.5$ ns is the PMT timing resolution.

The second step is to estimate the opening angle and direction. A goodness-of-fit is used to test the combination of the opening angle and direction:

$$Q(\theta_{edge}) = \frac{\int_0^{\theta_{edge}} \mathrm{PE}(\theta)d\theta}{\sin(\theta_{edge})} \times \left(\left.\frac{d\mathrm{PE}(\theta)}{d\theta}\right|_{\theta=\theta_{edge}}\right)^2 \times \exp\left(-\frac{(\theta_{edge} - \theta_{exp})^2}{2\sigma_\theta^2}\right) \tag{3.3}$$

Here $\mathrm{PE}(\theta)$ is the angular distribution of the observed charge as a function of opening angle $\theta$ (not the opening angle to be estimated, which is denoted as $\theta_{edge}$) at a certain direction, $\theta_{exp}$ is the expected Cherenkov opening angle given the charge within $\theta_{edge}$, and $\sigma_\theta$ is the angular resolution.

In the third step for vertex fitting, the vertex position will be fitted again using

the TDC-fit. This time photons are not assumed to be emitted from one point, but along the track length. Photon scattering is also taken into consideration. Finally, MS-fit is used to make a preciser fit[46]. In this fit, the information of ring pattern is used to search for the vertex position parallel to the direction. The upward-going muons are generated outside the ID, so their vertices are constrained on the surface of ID.

The momentum can be estimated using the number of observed Cherenkov photons inside a cone of 70° centered at the ring direction. However, the momentum estimated this way only includes the energy deposit in the detector. For UPMU, this is only the lower bound of the muon momentum, for the energy dissipated before reaching the ID, or even after leaving the ID for through-going and showering muons, is unknown. The estimated momentum is used as the energy for the UPMU events.

# CHAPTER 4

## Event Simulation

In this study, the background events dominate the data set where we search for the potential astrophysical neutrino events. The evidence for an existing neutrino point source is usually considered to be a cluster of multiple high-energy neutrinos in space and time. The spatial and time distribution of atmospheric neutrinos are supposed to be quite uniform in general, but could have coincident fluctuations which produce a false appearance looks like a signal. We cannot estimate the probability that such a situation occurs either by theoretical calculation or using the data we have collected, but we can use a powerful tool called Monte Carlo (MC) simulation to do it. MC simulates with three steps: atmospheric neutrino flux, neutrino interactions, and detector simulations. We will not directly use the simulation introduced in this chapter for this study. Instead, we use the already existed MC to generate a subset of toy MC events. Details of this will be talked about later in Section 5.4.1.

### 4.1 ATMOSPHERIC NEUTRINO FLUX

Atmospheric neutrinos are produced by CR. As mentioned in Section 1.4.1, the major components of CR are protons and nuclei such as $\alpha$-particles. These high-energy protons and $\alpha$-particles strike the atmosphere and interact with the nuclei isotropically, producing pions and kaons. Charged pions decay into muons and muon neutrinos:

$$\pi^- \to \mu^- + \bar{\nu}_\mu$$

$$\pi^+ \to \mu^+ + \nu_\mu$$

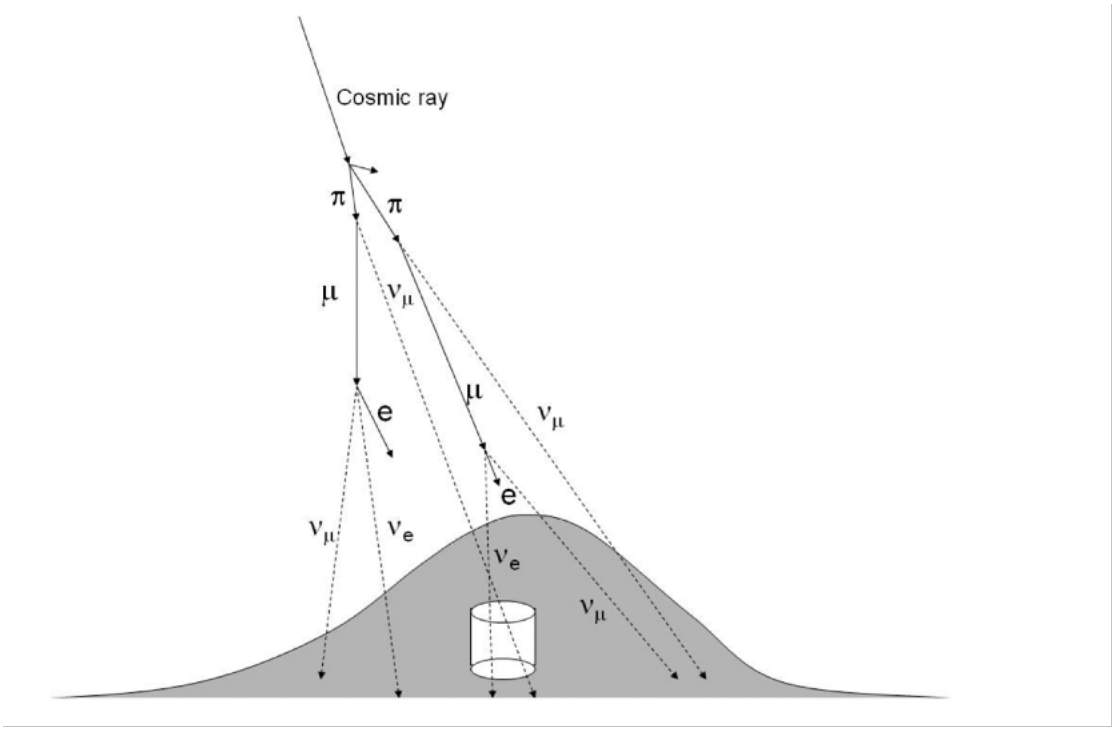


**Figure 4.1:** Schematic the creation of atmospheric neutrinos.[47]

and muons further decay into electrons, electron neutrinos and muon neutrinos:

$$\mu^+ \rightarrow e^+ + \nu_e + \bar{\nu}_\mu$$

$$\mu^- \rightarrow e^- + \bar{\nu}_e + \nu_\mu$$

The neutrino flux model SK uses is the Honda-Kajita-Kasahara-Midorikawa (HKKM) flux model[41]. HKKM model uses flux primary taken from experiments CR as input. Solar activity and geomagnetic field, which affect the flux of primary CR, are also taken into consideration. The theoretic models used for hadronic interaction between CRs and air nuclei are JAM and DPMJET-III. The particle interactions and propagation are calculated in three dimensions to enhance the near-horizon neutrino flux. A summary of the results from HKKM in comparison with Bartol flux[26] and Fluka

flux[27] are shown in Figure4.2.

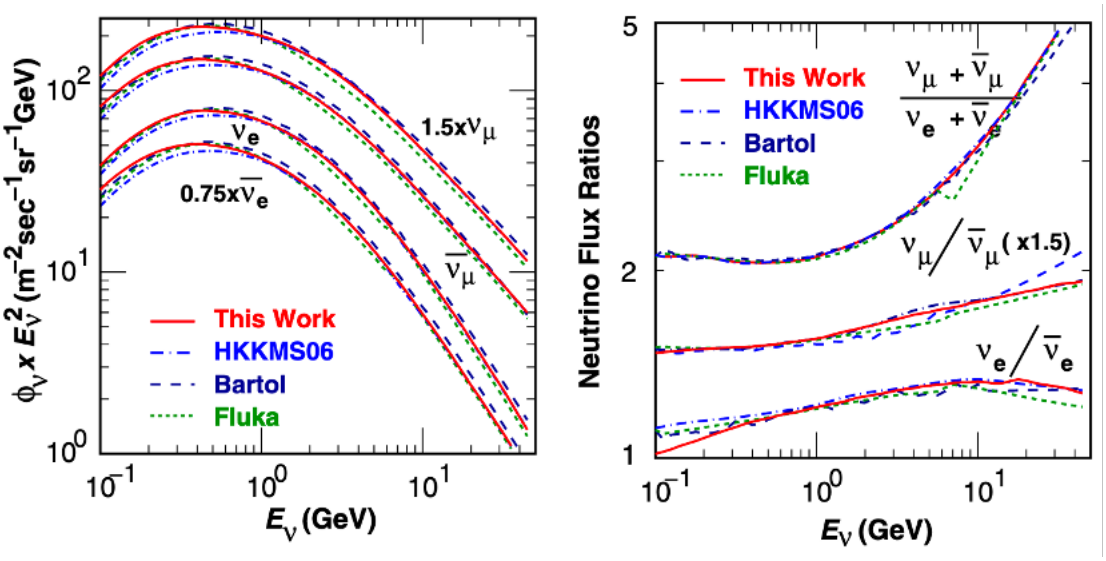


**Figure 4.2:** Left:Calculated atmospheric neutrino fluxes averaged over all directions for different models. Right: Neutrino and anti-neutrino flavor ratios for different models.[42]

## 4.2 NEUTRINO INTERACTION

Interaction between neutrinos and hydrogen and oxygen atom in water molecule and rock (primarily made of $SiO_2$) are simulated by NEUT[39]. According to the exchanged weak boson ($W^\pm$ or $Z$), the interactions are classified into charge current (CC) or neutral current (NC) two categories. The simulated interactions include:

| | |
|---|---|
| CC/NC Quasi-Elastic and Elastic Scattering | $\nu_l + N \rightarrow l/\nu_l + N'/N$ |
| CC/NC Single Meson and Gamma Production | $\nu_l + N \rightarrow l/\nu_l + N'/N + (\pi, K, \eta, \gamma)$ |
| CC/NC Deep Inelastic Scattering | $\nu_l + N \rightarrow l/\nu_l + N'/N + \text{hadrons}$ |
| CC/NC Coherent Pion Production | $\nu_l + {}^{16}\text{O} \rightarrow l/\nu_l + {}^{16}\text{O} + \pi$ |

where $N(N')$ is the nucleon (proton or neutron), $l$ is lepton (not include neutrinos) and $\nu_l$ is the neutrino for $l$.

For NC elastic scattering, no new particle is created, and the neutrino just scatters off a nucleon. The charged lepton that can be detected by SK is generated through CC quasi-elastic (CCQE) scattering. Llewellyn-Smith model[45] is used for CCQE cross-section of free protons. For nucleons bounded in an oxygen nucleus, Fermi motion and Pauli blocking of the nucleon are taken into account in model by Smith and Moniz[56].

A single meson can be produced via baryon resonance in the CC/NC neutrino-nucleon interaction. Such a simulation is based on the Rein and Sehgal model[54]. 18 resonances together with the pion-less delta-decay have been taken into consideration.

When neutrino energy exceed 10 GeV, the interactions between neutrino and quark in the nucleon which generate multiple hadrons via deep inelastic scattering (DIS) dominates the interactions. This is the dominant interaction for the upward-going muons. The cross section is by integrating $\frac{d^2\sigma}{dxdy}$, which is given by[39]:

$$\begin{aligned}\frac{d^2\sigma}{dxdy} =& \frac{G_F^2 M_N E_\nu}{\pi}\left\{(1-y+\frac{1}{2}y^2+C_1)F_2(x,q^2)\right. \\ & \left.\pm y(1-\frac{1}{2}y+C_2)[xF_3(x^2,q^2)]\right\}\end{aligned} \tag{4.1}$$

$$C_1 = \frac{yM_l^2}{4M_N E_\nu x} - \frac{xyM_N}{2E_\nu} - \frac{M_l^2}{4E_\nu^2} - \frac{M_l^2}{2M_N E_\nu x} \tag{4.2}$$

$$C_2 = -\frac{M_l^2}{4M_N E_\nu x} \tag{4.3}$$

Here, $x = -q^2/(2M(E_\nu - E_l))$, $y = (E_\nu - E_l)/E_\nu$, $M_n$ and $M_l$ are the mass of the nucleon and lepton, respectively, $E_\nu$ and $E_l$ are energies of the incoming neutrino and outgoing lepton in laboratory frame. $F_2$ and $xF_3$ are the nucleon structure functions taken from GRV98[36]. Figure 4.3 shows the calculated total charged current cross section in comparison with the experiment data.

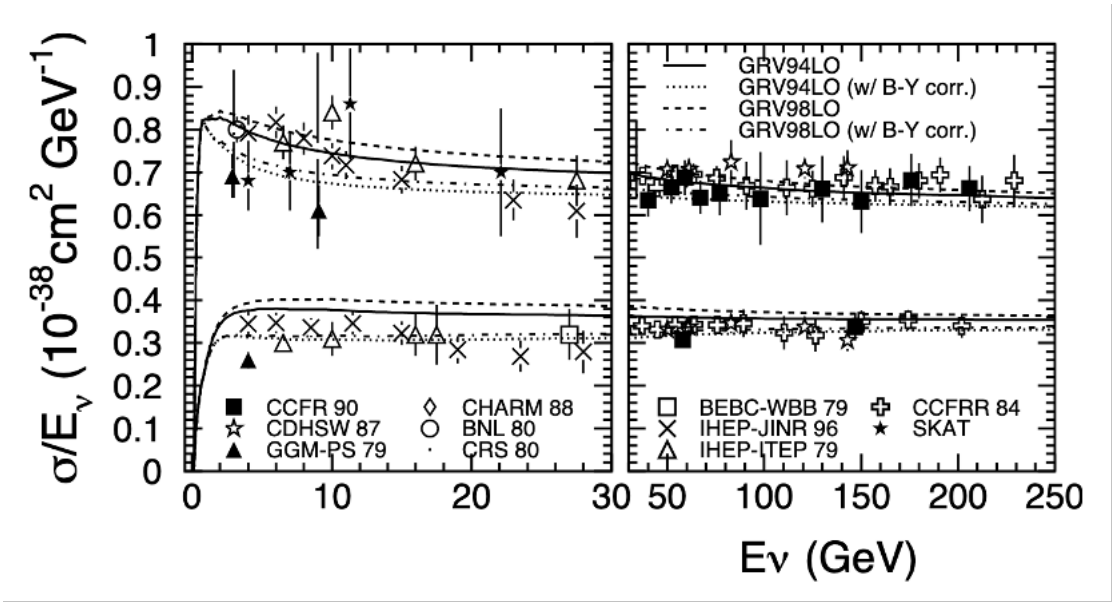


**Figure 4.3:** Total charged current cross sections for neutrinos (top 4 lines) and antineutrinos (bottom 4 lines).[39]

Beside the baryon resonance, a pion can also be produced by the interaction between neutrino and oxygen nucleus called coherent pion production. Such an interaction is also simulated in Rein and Sehgal model.

## 4.3 DETECTOR SIMULATION

The detector simulations include particle propagation, Cherenkov photon generation and propagation, and PMT response. These are simulated by a GEANT3 based package, SKDETSIM.

For hadronic interactions except for low energy pions, GCALOR[64] is used. Low energy pions are simulated using a custom program[50]. Charged particle propagation are simulated based on what we discussed in Section 2.2.

In Cherenkov photon propagation simulations, Rayleigh scattering, Mie scattering and absorption by water molecule are considered. Reflection on the wall of the tank is also calculated.

PMT charge and time response simulation use the measurements from calibration.

# CHAPTER 5

## Analysis

### 5.1 DATA SAMPLE

In this study, we look for the high-energy astrophysical neutrino point sources in SK-IV using only UPMU events. We used 4547 UPMU events from SK-IV with a total live time of 3288.8 days for the analysis, and also the MC equivalent to 500.0 years simulation are used for the calculation of the PDF in Section 5.2.2 and the generation of the toy MC in Section 5.4.1. Figure 5.1 shows a sky map of all UPMU events and Figure 5.2 is the time distribution of all UPMU events.

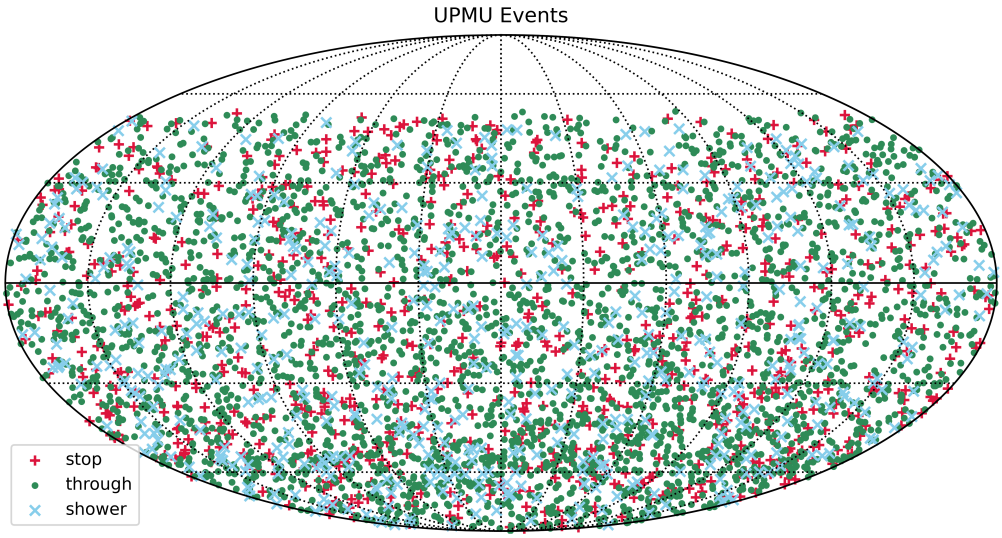


**Figure 5.1:** A sky map of different types of UPMU events. All the sky map in this and next chapter are shown in J2000 equatorial coordinate.

Since we are searching the full sky without relying on any other triggers, it is very important to have good angular resolutions for all the events we use. As shown in 5.3, UPMU events have the best angular resolution among the all three samples.

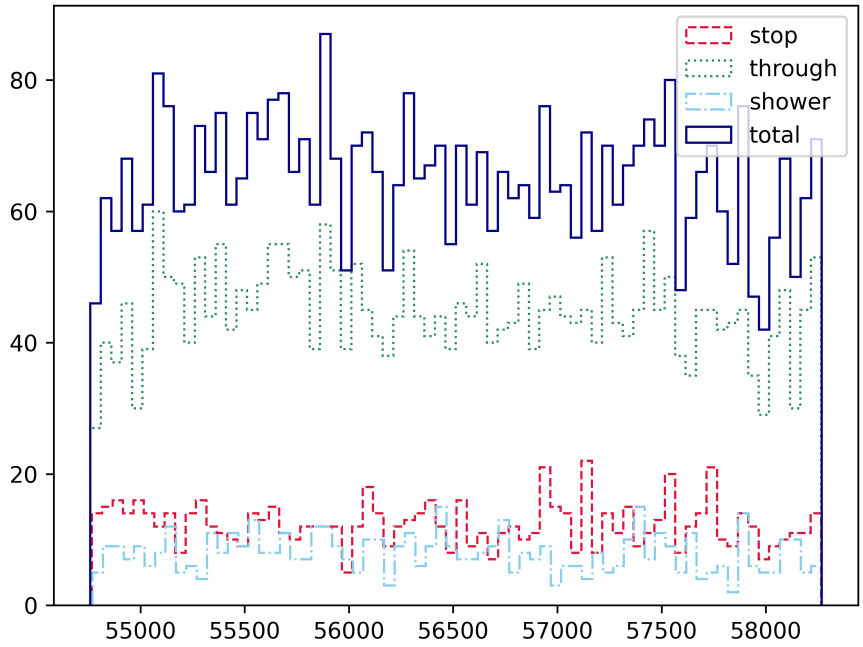


**Figure 5.2:** Time distribution of different types of events. Time is presented in the modified Julian day (mjd).

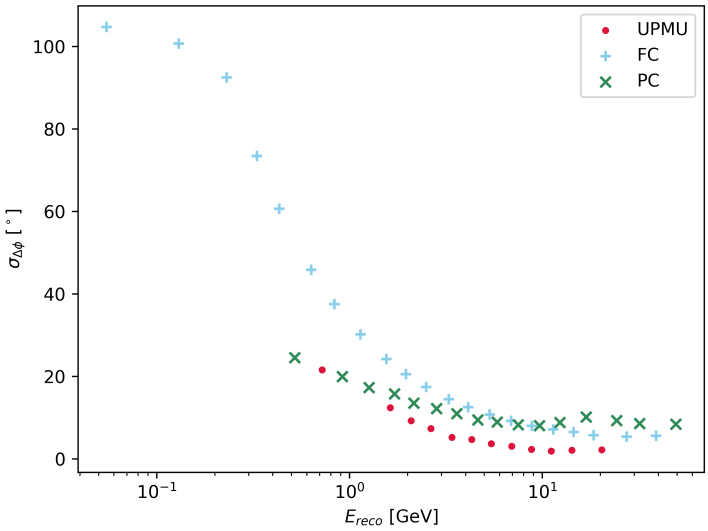


**Figure 5.3:** Angular resolution corresponding to $1\sigma$ for FC, PC and UPMU from atmospheric neutrino simulation.

## 5.2 UNBINNED MAXIMUM LIKELIHOOD METHOD

### 5.2.1 Likelihood

In this study, events are classified into two categories: either a signal event or a background event. For the data set we use, there are two hypothesis: a null hypothesis which means no signal events is in the data set, and another hypothesis that at least one signal event is in the data set. The direction, energy and time PDF for the signal and background events are different.

For the binned method, events within a certain angular region and time interval around the assumed source direction and burst time are selected. This region and interval can be chosen based on the detector angular resolution and burst model. By comparing the number of selected events and the expected background events, we can get the probability of having such a number of events without any signal events. Then we can evaluate the expected number of signal events if the probability is lower

than a confidential level threshold.

For the unbinned method that is used in this study, each event does not have to be taken as either a signal or a background. Instead, it is a combination of a signal component and a background component. The probability density for $i^{th}$ event in a set of N events is:

$$\frac{n_S}{n_S + n_B} S_i + \frac{n_B}{n_S + n_B} B_i \tag{5.1}$$

Then the likelihood for N events is:

$$\mathcal{L} = \frac{e^{n_S + n_B} (n_S + n_B)^N}{N!} \prod_{i=1}^{N} \left( \frac{n_S}{n_S + n_B} S_i + \frac{n_B}{n_S + n_B} B_i \right) \tag{5.2}$$

Here the $n_S$ ($n_B$) is the expected number of signal (background) events, $S_i$ ($B_i$) is the signal (background) probability density function (PDF). $n_S$ is the only unknown variable here, so we can fit $n_S$ to maximize $\mathcal{L}(n_S)$ and obtain the expected number of signal events.

Both binned and unbinned methods are top-down searches and are model independent. This is a much more efficient choice compared with the bottom-up search, as there are too many possible models to test, but little progress has been obtained.

In this study we will conduct both a time-integrated search and a time-dependent search for high-energy astrophysical neutrino point sources. These two methods have advantages in different neutrino emission duration. Time-integrated search have a better performance for sources with emission duration longer than 100 days, while time-dependent search will have a better discovery potential for shorter time duration[4].

When calculating the likelihood, if all events are included, it will take an extremely long time. This is neither efficient nor necessary. The angular resolution for

UMPU have been discussed in Section 5.3 and it can be seen in Figure5.3 that events reconstructed to energy above 1 GeV have angular resolution smaller than 15°. As a result, it is reasonable for us to calculate likelihood with only events within a search cone centered at the source direction with an opening angle of 15°.

### 5.2.2 Variables

Before introducing PDF, it is important to take a look at the variables that will be used in the searching algorithm. In time-integrated search, only angular and energy PDF will be included in the likelihood Equation 5.3 and we calculate $\mathcal{L}(n_S, \gamma)$ as a function of $n_S$ and energy spectrum index $\gamma$. For time-dependent search, Equation 5.2 will also consist of a time PDF, and $\mathcal{L}(n_S, \gamma, t_0, \sigma_t)$ is calculated as a function of two extra parameter, emission center time $t_0$ and emission duration $\sigma_t$. Details on this will be discussed in the following section.

The $S_i$ and $B_i$ in Equation 5.3 is given as

$$S_i = \mathcal{A}_i^S(\Delta\phi_i|E_i)\mathcal{E}_i^S(E_i|\gamma) \tag{5.3}$$

$$B_i = \mathcal{A}_i^B(dec_i|dec_0)\mathcal{E}_i^B(E_i) \tag{5.4}$$

for time-integrated search and

$$S_i = \mathcal{A}_i^S(\Delta\phi_i|E_i)\mathcal{E}_i^S(E_i|\gamma)\mathcal{T}_i^S(t_i|t_0, \sigma_t) \tag{5.5}$$

$$B_i = \mathcal{A}_i^B(alt_i|dec_0)\mathcal{E}_i^B(E_i)\mathcal{T}_i^B \tag{5.6}$$

for time-dependent search. Here $\mathcal{A}_i^{S(B)}$, $\mathcal{E}_i^{S(B)}$ and $\mathcal{T}_i^{S(B)}$ are the angular PDF, energy PDF and time PDF for signal (background).

The definition of each variable is listed below:

- $\Delta\phi_i$: the angular separation between reconstructed direction of $i^{th}$ muon event and assumed point source in equatorial coordinate.
- $dec_0$: declination of assumed point source in equatorial coordinate.
- $E_i$: reconstructed energy of $i^{th}$ muon event.
- $\gamma$: spectrum index.
- $dec_i$: declination of $i^{th}$ muon event in equatorial coordinate.
- $alt_i$: altitude of $i^{th}$ muon event in detector coordinate.
- $t_i$: detection time of $i^{th}$ muon event.
- $t_0$: center of neutrino emission time.
- $\sigma_t$: duration of neutrino emission.

### 5.2.3 Probability Density Function

It is important to notice that the PDF time-integrated search and time-dependent search do not only differ in the time part, but also have a difference in the angular part for background. The PDF are calculated using the MC.

The angular PDF of signal events depends on their reconstructed energy. The energy interval used for this study is divided into bins with same number of events in each bin. The distribution of the scattering angles between the reconstructed direction of muons and the true direction of the neutrinos are fitted with a Gaussian-like function in each bin. Then the PDF is normalized between 0° and 15°. Azimuth ($\varphi$) distribution is taken to be uniform. Plots of $\mathcal{A}^S(\Delta\phi|E_\mu) = P(\Delta\phi|E_\mu)P(\varphi)$ is shown is in Figure 5.4.

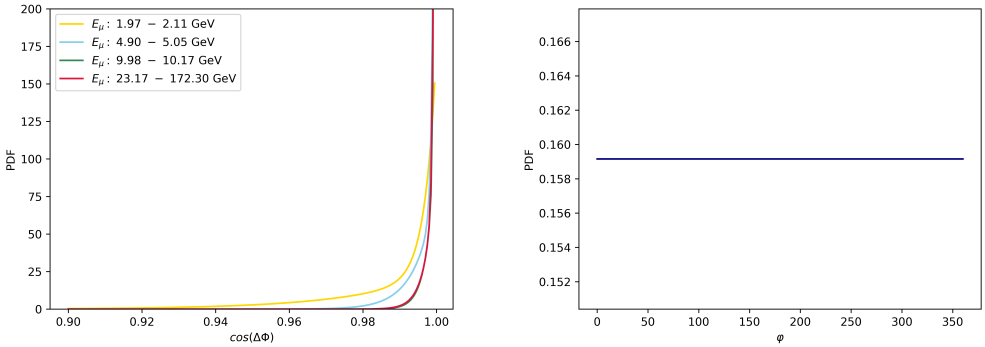


**(a)** **(b)**

**Figure 5.4:** $\mathcal{A}^S(\Delta\phi|E_\mu)$ for signal events at different reconstructed energy. Left: $P(\Delta\phi|E_\mu)$. Right: $P(\varphi)$

It is more complicated for the background angular PDF. Using the MC, we can obtain the angular PDF in the detector coordinate. But when we are searching for astrophysical point sources, we look for them in the equatorial coordinate. There is an one-to-one correspondence between the altitude and azimuth, and declination and right ascension for a given local sidereal time. Thus we can calculate the declination PDF in the following way:

$$\begin{aligned} P(dec, ra) &= \int_0^{24} P(dec, ra, t)dt \\ &= \int_0^{24} P(alt, azi, t)dt \\ &= \int_0^{24} P(alt)P(azi)P(t)dt \end{aligned} \tag{5.7}$$

Here $P(alt)$ and $P(azi)$ are the altitude and azimuth PDF in the detector coordinate (Figure 5.5) and $P(t)$ is the local sidereal time (lst) distribution (Figure 5.6). The integration of $P(t)$ and Jacobian matrix equal to 1, hence are omitted here.

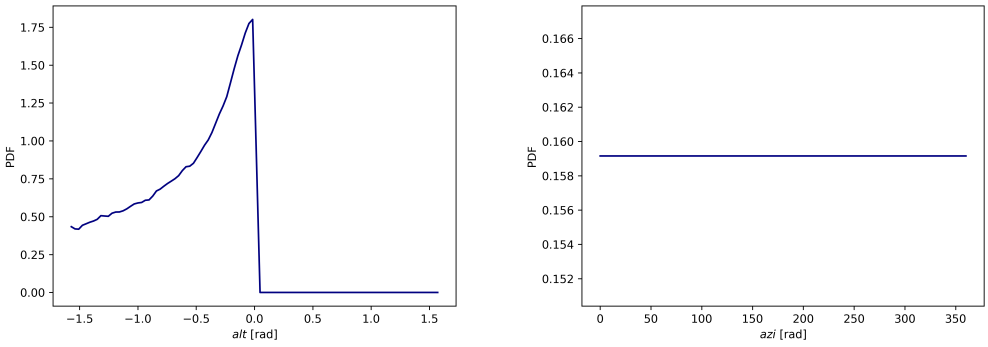


**(a)** **(b)**

**Figure 5.5:** $\mathcal{A}^B(dec, ra)$ for background events used in time-dependent search. Left: $P(alt)$. Right: $P(azi)$.

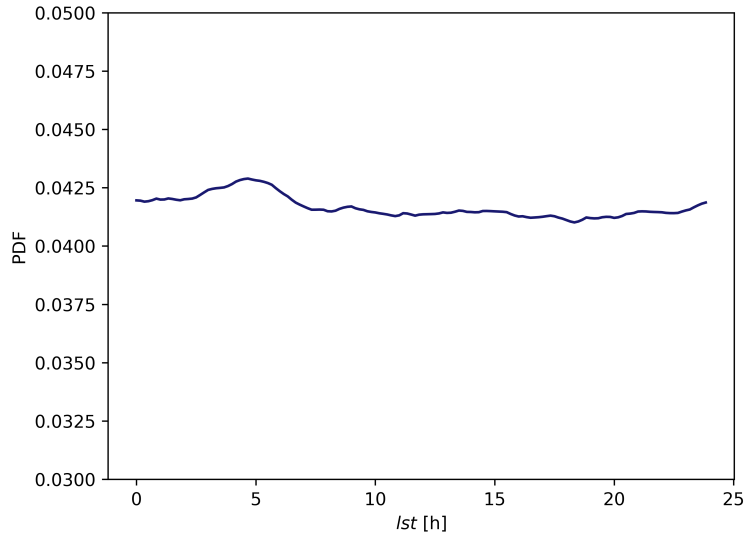


**Figure 5.6:** Local sidereal time (LST) distribution.

Taking the right ascension distribution to be uniform, we have $\mathcal{A}^B(dec) = P(dec)P(ra)$ (Figure 5.7). The probability of being inside the search cone is:

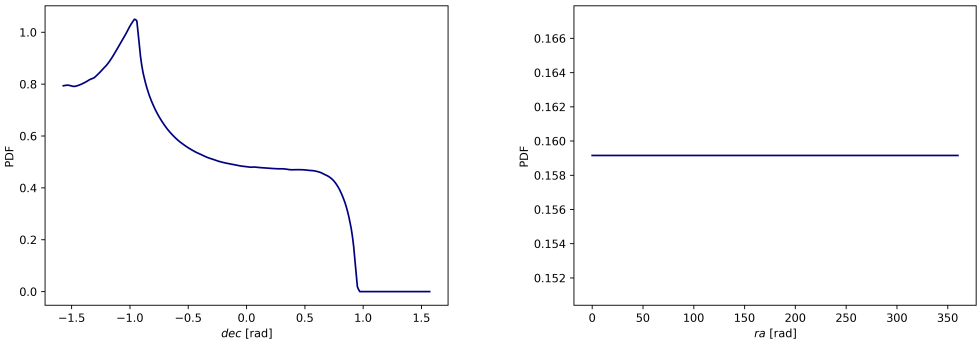


**(a)** **(b)**

**Figure 5.7:** $\mathcal{A}^B(dec, ra)$ for background events used in time-integrated search. Left: $P(dec)$. Right: $P(ra)$.

$$P((dec, ra) \in \{\Delta\phi(dec, ra) \leq 15^\circ\}) = \int_{\Delta\phi(dec,ra)\leq 15^\circ} P(dec, ra)\cos(dec)d(dec)d(ra) \tag{5.8}$$

And eventually we have the angular PDF with the precondition of being in the search cone for time-integrated search:

$$\begin{aligned} \mathcal{A}^B(dec|dec_0) &= P(dec, ra|\Delta\phi(dec, ra) \leq 15^\circ\}) \\ &= P(dec)P(ra)/P((dec, ra) \in \{\Delta\phi(dec, ra) \leq 15^\circ\}) \end{aligned} \tag{5.9}$$

Things are, on the other hand, a bit different for the time-dependent search, since variables in $P(dec, ra, t)$ are correlated. We have to calculate the PDF in the following

way:

$$
\begin{aligned}
P(dec, ra, t|\Delta\phi(dec, ra) \leq 15^\circ\}) &= P(dec, ra|(dec, ra) \in \{\Delta\phi(dec, ra) \leq 15^\circ\}, t)P(t) \\
&= \frac{P(dec, ra, (dec, ra) \in \{\Delta\phi(dec, ra) \leq 15^\circ\}|t)P(t)}{P((dec, ra) \in \{\Delta\phi(dec, ra) \leq 15^\circ\})} \\
&= \frac{P(dec, ra|t)P(t)}{P((dec, ra) \in \Delta\phi(dec, ra) \leq 15^\circ\})} \\
&= \frac{P(dec, ra, t)}{P((dec, ra) \in \{\Delta\phi(dec, ra) \leq 15^\circ\})} \\
&= \frac{P(alt, azi, t)}{P((dec, ra) \in \{\Delta\phi(dec, ra) \leq 15^\circ\})} \\
&= \frac{P(alt)P(azi)P(t)}{P((dec, ra) \in \{\Delta\phi(dec, ra) \leq 15^\circ\})}
\end{aligned}
\tag{5.10}
$$

The angular PDF with the precondition of being in the search cone for time-dependent search is given by:

$$
\mathcal{A}^B(alt|dec_0) = P(alt)P(azi)/P((dec, ra) \in \{\Delta\phi(dec, ra) \leq 15^\circ\}) \tag{5.11}
$$

The energy distribution of high-energy astrophysical neutrinos has not been confirmed experimentally, so we assume they follow a spectrum distribution, but leave the spectrum index free to change in a range. With this, we can calculate the energy PDF of signal event:

$$
\mathcal{E}(E_\mu, \gamma) = \int\int E_\nu^{-\gamma} P(E_\nu, E_\mu^{min}) S(z, E_\nu) f(E_\mu|E_\nu) dE_\nu dz/N \tag{5.12}
$$

N is the normalization factor.

The first part we need is the probability that a neutrino of energy $E_\nu$ is scattered off into a muon with an energy larger than the minimum energy $E_\mu^{min}$ to be detected as an UPMU event $P(E_\nu, E_\mu^{min})$ (Figure 5.8). We also need to take into account the

earth shadow effect $S(z, E_\nu)$ (Figure 5.9), where $z \equiv cos(\theta)$ and $\theta$ is the zenith angle in the detector coordinate.

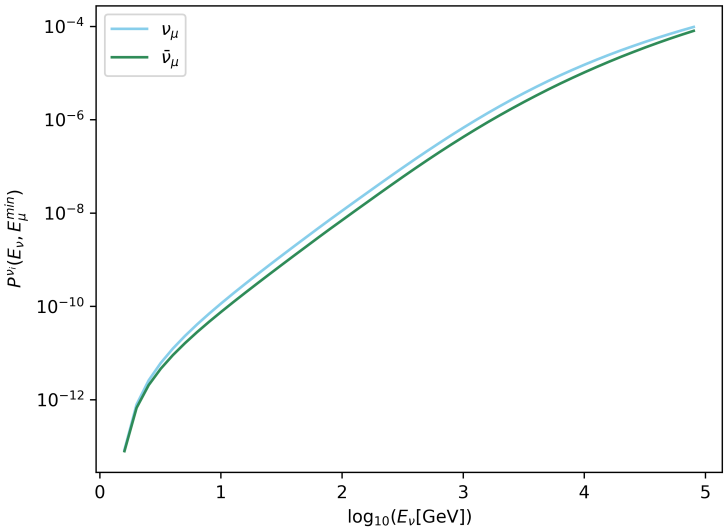


**Figure 5.8:** Probability $P(E_\nu, E_\mu^{min})$ for a neutrino of energy $E_\nu$ creating a muon of energy larger than $E_\mu^{min}$.

Then we calculate the energy response function $f(E_\mu|E_\nu)$ (Figure: 5.10), which is the probability of a neutrino of $E_\nu$ being reconstructed to an UPMU event of $E_\mu$. Just like what we did when calculating the angular PDF for signal events, we divide the energy interval of MC into small bins, yet the reconstructed energy is changed to neutrino energy. In each bin, we calculate the PDF of reconstructed energy.

Background energy PDF can simply be obtained from the MC. Figure 5.11 shows a comparison of the $\mathcal{E}^S(E_\mu, \gamma)$ and $\mathcal{E}^B(E_\mu)$.

Shape of signal time PDF is also unknown to us, so here we use the Gaussian distribution

$$\mathcal{T}(t_i|t_0, \sigma_t) = \frac{1}{\sigma\sqrt{2\pi}} e^{-\frac{1}{2}\left(\frac{t_i - t_0}{\sigma}\right)^2} \tag{5.13}$$

and leave $t_0$ and $\sigma_t$ as free parameters to be fitted. For background time PDF, we

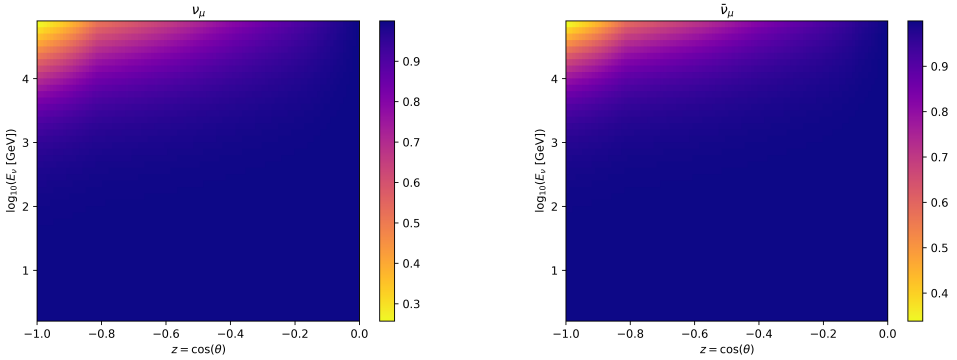


**(a)** **(b)**

**Figure 5.9:** Earth shadow effect $S(z, E_\nu)$ for $\nu_\mu$ (left) and $\bar{\nu}_\mu$ (right) as a function of $\log_{10} E_\nu$ and $z = \cos\theta$.

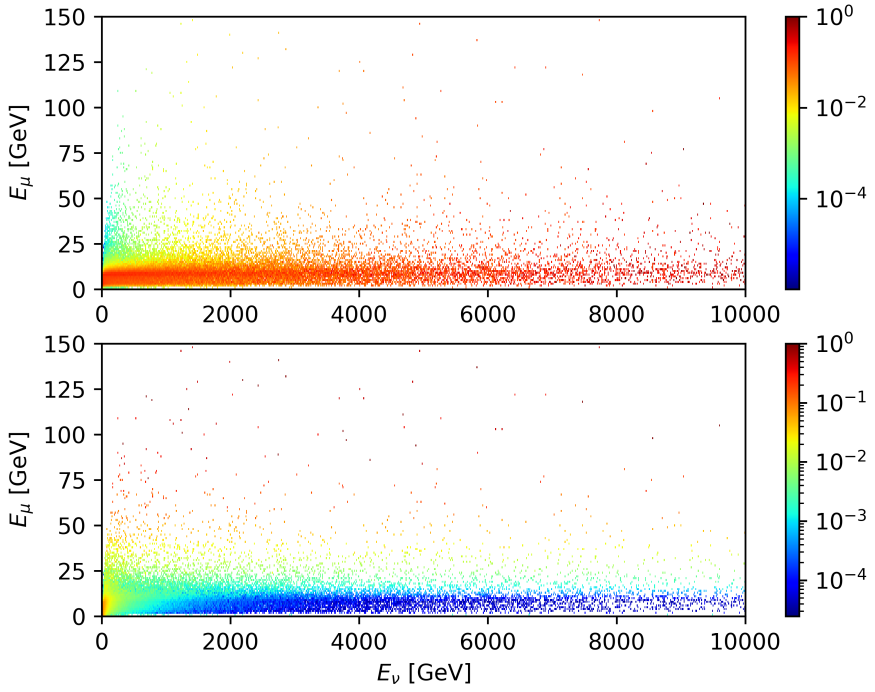


**Figure 5.10:** Top: The probability that a neutrino of energy $E_\nu$ creates a muon of reconstructed energy $E_\mu$ ($f(E_\mu|E_\nu)$).Bottom: The probability that a muon of reconstructed energy $E_\mu$ is created by a neutrino of energy $E_\nu$

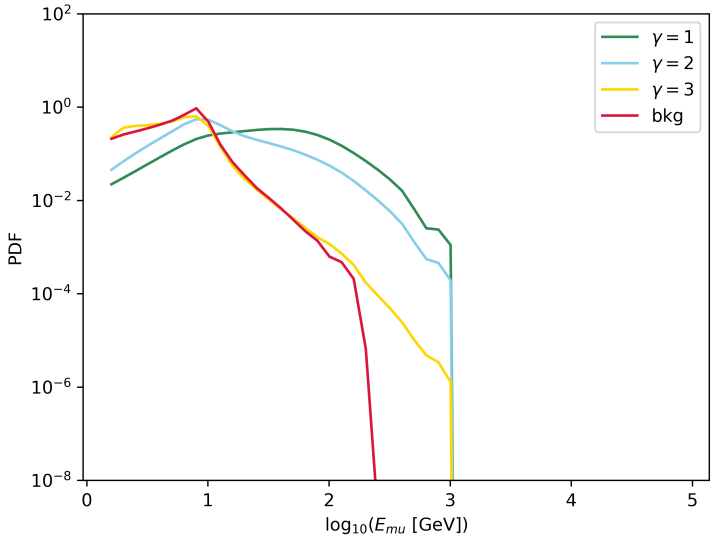


**Figure 5.11:** Expected reconstructed energy distribution for background events and signal events with different spectrum indices.

assume it to be uniformly distributed $\frac{1}{T_{end}-T_{start}}$, where $T_{end} - T_{start}$ is the operation time of SK-IV (not live time). (Figure 5.12)

### 5.2.4 Expected Number of Background Events

SK receives atmospheric neutrino events at a quite stable event rate in each direction. This again is in the detector coordinate. In order to calculate the expected number of background events in the search cone, we need to transform to equatorial coordinate. By assigning local sidereal time to each event in MC according to the distribution, we can calculate their corresponding declination and right ascension. Then we count the number of events within the search cone at all searching directions. Finally, all $n_B$ are weighted by $\frac{T_{SK-IV}}{T_{MC}}$, data and MC live time ratio. In Figure 5.13, a comparison between the calculated expected $n_B$ and the true event distribution of the SK-IV data is shown, together with the $n_B$ as a function of declination averaged over right

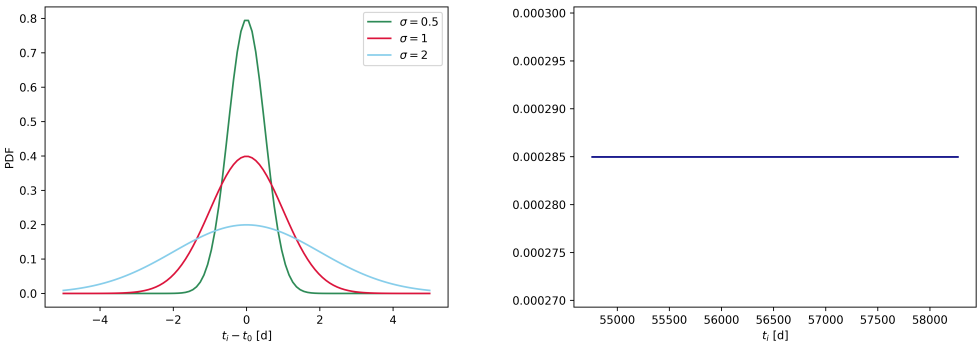


**(a)** **(b)**

**Figure 5.12:** $\mathcal{T}^S(t|t_0, \sigma_t)$ for signal (left) and $\mathcal{T}^B$ for background (right)

ascensions.

### 5.2.5 Test Statistics

We have defined the likelihood in a general sense in Section 5.2.1. In order to calculate the probability that such a situation is generated by the fluctuation of background events, we need to make a comparison with the null hypothesis ($n_S = 0$). To do so, we can calculate the ratio of two likelihood and define it as the test statistics ($TS$). The $TS$ for time-integrated search is defined as:

$$\begin{aligned} TS &= 2\log\left[\frac{\mathcal{L}(\hat{n}_S, \hat{\gamma})}{\mathcal{L}(n_S = 0)}\right] \\ &= 2\sum_{i=1}^{N}\log\left(1 + \frac{n_S S_i}{n_B B_i}\right) - 2n_S \end{aligned} \tag{5.14}$$

where $\hat{n}_S$ and $\gamma$ are the best fitted number of signal events and the energy spectrum index. The probability of observing a given $TS$ with null hypothesis will approximately accord to the $\chi^2$ distribution.

In the time-dependent search, we must pay attention to a not so obvious fact which

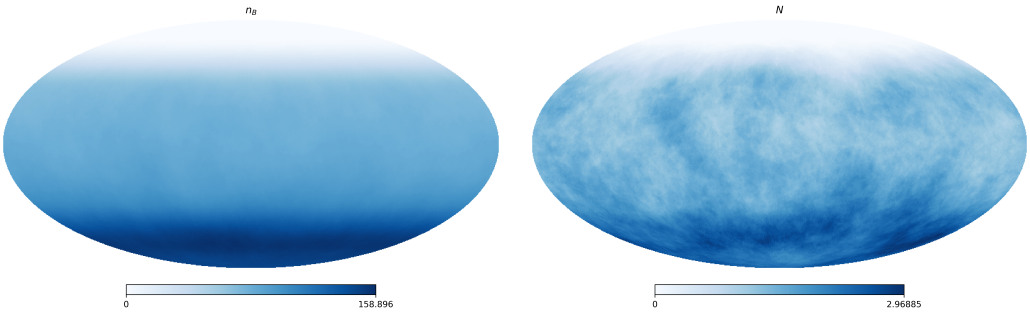


**(a)** **(b)**

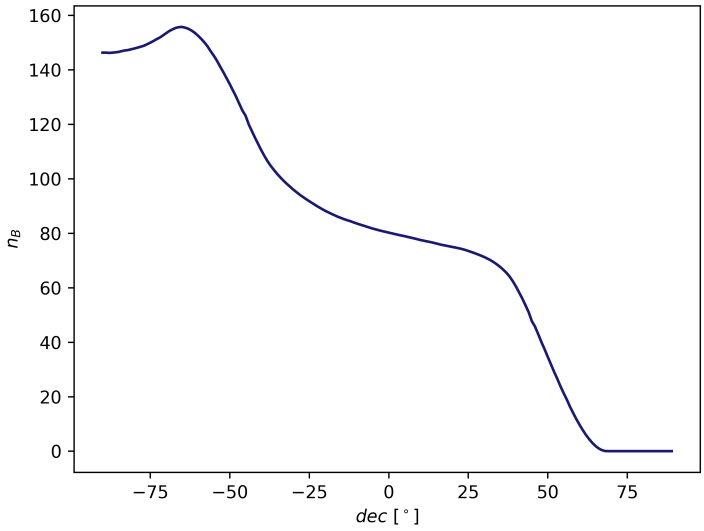


**(c)**

**Figure 5.13:** Top left: Sky map of expected number of background events within the search cone. Top right: Sky map of number of events within the search cone for the data. Bottom: Expected number of background events as a function of declination.

is easy to be neglected. For background events with a uniform time distribution, the probability for $n_B$ events to be within $2\sigma_t$ is smaller for shorter $\sigma_t$. On the other hand, if $\sigma_t$ becomes shorter, $\mathcal{T}(t_i|t_0,\sigma_t)$ will have a larger peak value. As a result, the algorithm will prefer a shorter $\sigma_t$, which is reasonable. Yet we must also realize another aspect that for the same searching period, the number of independent ways of choosing $t_0$, or in another way of saying, the number of non-overlapping region with a time width of $2\sigma_t$ is larger for shorter $\sigma_t$, meaning that the probability that $n_B$ background events appear within at least one of the time region becomes larger.

In order to include this effective trail factor in the algorithm, we can integrate the likelihood over all possible $t_0$ for a given $\sigma_t$:

$$\mathcal{L}(n_S,\gamma,\sigma_t) = \frac{1}{T_{end}-T_{start}} \int_{T_{start}}^{T_{end}} \mathcal{L}(n_S,\gamma,\sigma_t,t_0)dt_0 \tag{5.15}$$

The integral can be approximated by a penalty term times the maximized original likelihood[29]:

$$\mathcal{L}(\hat{n}_S,\hat{\gamma},\hat{\sigma}_t) \sim \frac{\sqrt{2\pi}\hat{\sigma}_t}{T_{end}-T_{start}} \mathcal{L}(\hat{n}_S,\hat{\gamma},\hat{\sigma}_t,\hat{t}_0) \tag{5.16}$$

Where $T_{end}$ and $T_{start}$ are the ending and starting time of SK-IV. Ignoring the constant $\sqrt{2\pi}$, the modified $TS$ then becomes:

$$\begin{aligned} TS &= 2\log\left[\frac{\hat{\sigma}_t}{T_{end}-T_{start}} \times \frac{\mathcal{L}(\hat{n}_S,\hat{\gamma},\hat{\sigma}_t)}{\mathcal{L}(n_S=0)}\right] \\ &= 2\sum_{i=1}^{N} \log\left(1+\frac{n_S S_i}{n_B B_i}\right) - 2n_S + 2\log\left(\frac{\sigma_t}{T_{end}-T_{start}}\right) \end{aligned} \tag{5.17}$$

## 5.3 ALL-SKY SEARCH

So far we have discussed the construction of $TS$ and its elements in details. Our next step is to obtain the value of the free parameters that maximize the likelihood and the corresponding $TS$ at each searching direction. In general, we will carry out the all-sky search in the following steps:

1. Obtain the best fitted $\hat{n}_S$, $\hat{\gamma}$, $\hat{t}_0$ and $\hat{\sigma}_t$ which maximize $\mathcal{L}$ and the corresponding $TS$ at each direction.

2. Find the direction with the overall maximum $TS_{max}$, together with its corresponding $\hat{n}_S$, $\hat{\gamma}$, $\hat{t}_0$ and $\hat{\sigma}_t$.

We will discuss the detail procedures for each step in the following sections.

### 5.3.1 Parameters Fitting and Likelihood Maximization

We will maximize the likelihood numerically because the energy PDF of signal and its dependence on $\gamma$ is obtained numerically, and there are to many terms contained in the likelihood. But the PDF of signal part can be extremely large and exceed the maximum limit of number storage for a signal like event, so instead we will minimize the minus logarithm likelihood, which has opposite monotonicity and same extreme point as the original likelihood.

As has been mentioned in previous sections, the events we are looking at are background dominated, which means in most of the cases, $n_S$ will be fitted to be 0. The number of events within the search cone at a given direction $N$ will fluctuate so it is possible for that number to be smaller than the expected number of background events $n_B$, and the likelihood will maximize at negative $n_S$ to make up the "missing"

events in the search cone. We are not interested in such a situation, so the lower limit of $n_S$ is set to be zero (see Figure 5.14).

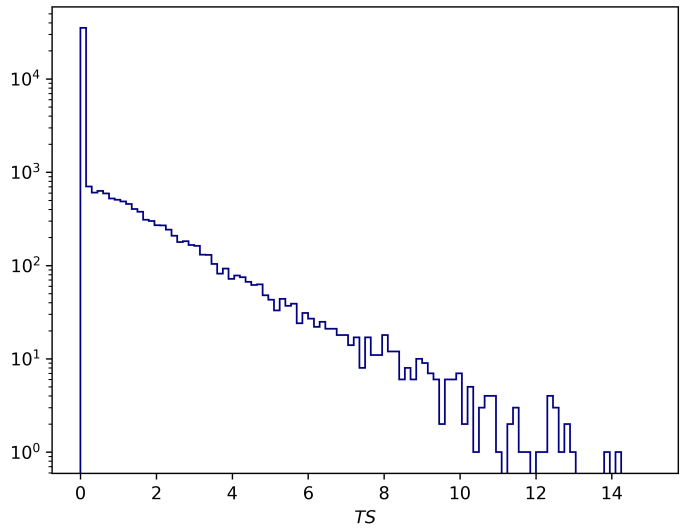


**Figure 5.14:** $TS$ distribution for time-integrated search in a pseudo experiment with solely background toy MC.

### 5.3.2 First Guess of Time Parameters

The minimizer we use here is `iminuit`. This minimizer is powerful to find the local maximum (it is supposed to be the minimum not maximum, but since the minimum of minus logarithm likelihood corresponds to the maximum of likelihood, I will use maximum instead for convenience) if given an accurate initial value. For the time-integrated search, it is expected that there is only one local maximum, so this maximum is the global maximum. On the other hand, a large amount of local minima may exist in the time-dependent search, especially when $\sigma_t$ is small, as shown in Figure 5.15. If we set the initial value of $t_0$ to be $T_{start}$ or $T_{end}$, this minimizer will return the first or last local maximum in the search time region, which does not

necessarily to be the global maximum. As a result, we must make an accurate enough first guess of $t_0$ and $\sigma_t$, and use them as the initial value for the fit.

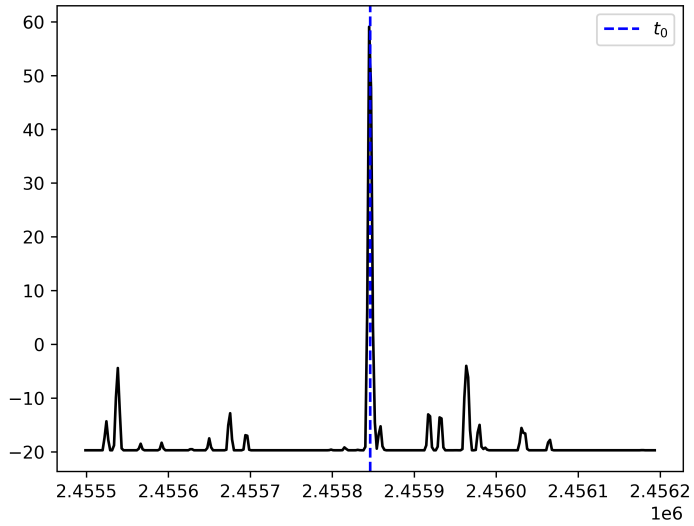


**Figure 5.15:** $TS$ as a function of $t_0$ with fixed $\sigma_t$ in a pseudo experiment using toy MC. Vertical dashed blue line represents the assumed emission center time. Simulated with $n_S = 10$ on top of the background toy MC, $\sigma_t = 10^5$s, at $dec = 30°$.

A method to obtain the first guess values is intro[29] and is adjusted for this study. To do so, only a part of the events in the search cone are needed because those far away from the source does not have much effect on fitting the time parameters. After balancing between the accuracy and calculation speed, we decide to use events within 7.5° from the searching direction. Then we arrange these events in time order, and divide them into groups. The $i$th group contains $n$ consecutive events from the $i$th to the $(i + n - 1)$th. Here $n$ is an integer in range $[2, 8]$, as the results hardly change for $n > 8$. For each group of each $n$, we calculate the likelihood with $n$ as $n_S$, $t_0$ and $\sigma_t$ as the mean value and standard deviation of $t_i$ respectively and fixing $\gamma$ to 2. And finally we use the $t_0$ and $\sigma_t$ corresponding to the overall largest likelihood as the first

guess value.

### 5.3.3 Search Directions

In order to do the all-sky search for the point sources, we need to divide the full sky into small bins. A usual way to do this is to use the equally sliced grids in equatorial coordinate, for example $1^\circ \times 1^\circ$ grids. This, however, has a disadvantage that the corresponding solid angle of each grid will decrease as the declination gets larger, making the angular uncertainties of the search nonuniform. An improved way that has been widely used by astronomy research is HEALPix method[3], which will divide the full sky into pixels with the same solid angle. Fig5.16 shows an example of how it works. The searching directions are set to be the positions of pixel centers. In principle, the trial factor will become larger if we more searching directions, as

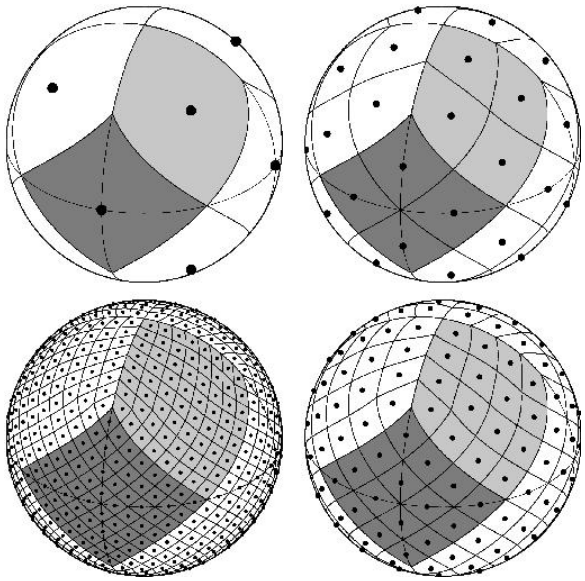

**Figure 5.16:** A schematic of how HEALPix divide the full sky into pixels.[3]

the probability for at least one $TS$ in all directions is larger than a certain value increases. The number of pixels that full sky is divided into is eventually decided to

be 49152 with an separation between two pixels being 0.5°. This is smaller than the best angular resolution for the highest-energy events of SK, and reduce the possibility of the clustering of point sources in one pixel as well.

After calculating $TS$ for all searching directions, we get a sky map of $TS$, as shown in Figure 5.17.

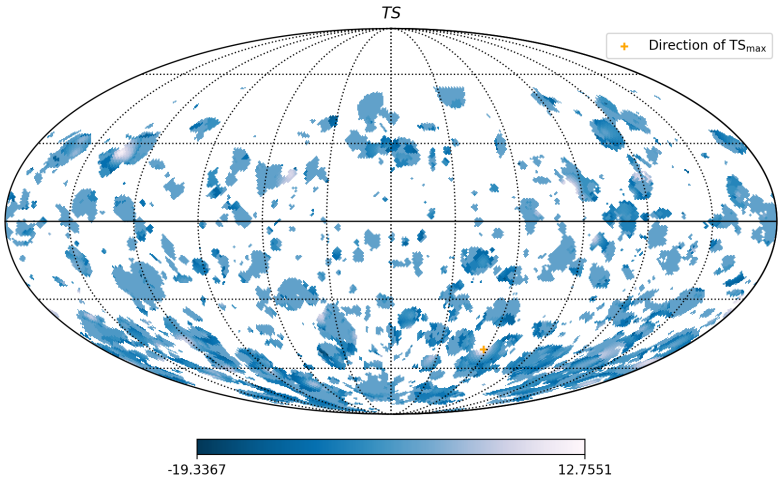


**Figure 5.17:** A sky map of $TS$ for time-dependent search in pseudo experiment with solely background toy MC.

## 5.4 PSEUDO EXPERIMENTS

After performing the full sky time-integrated and time-dependent search, we need to estimate the significance of the result with respect to the background. To do so, we calculate two different $p$-values using the results from simulation. The pre-trial $p$-value is calculated by comparing $TS_{max}$ with the distribution of $TS$ from the same position obtained by simulating using toy MC $10^6$ from trials. In order to take into account this trial factor, we also need to calculate the post-trial $p$-value. To do so, we first run many pseudo experiments called the trials and get a distribution of $TS_{max}$

in each trial. Then we compare the $TS_{max}$ we obtain from the data with this and calculate the post-trial $p$-value. In this section, I will introduce how to run the trials.

### 5.4.1 Toy Monte Carlo

A set of simulated events is needed to be thrown for each trial. We can generate the so called toy MC, which only contains the required information for the PDF. Each variable in the toy MC will follow the distribution calculated from the MC in Chapter 4.

We generate one background toy MC in the following procedure:

1. Assign energy according to the distribution shown in Figure 5.11.
2. Assign altitude and azimuth according to the distribution in Figure 5.7 or 5.5.
3. Assign Julian date with the following steps:
   (a) Choose which run the event is in. Each run is weighted by its duration times its live time rate.
   (b) Assign a time in the duration of that run assuming a uniform distribution.
4. Calculate the equatorial coordinates (right ascension and declination).

The number of background toy MC events follows Poisson distribution, with the mean value being the event rate times total live time for SK-IV.

Besides the threshold of $TS$, we also what to evaluate the sensitivity of this searching algorithm for SK. This not only requires events sets containing solely backgrounds, but also several signals on top of backgrounds. Before generating signal toy MC, we need to determine the direction and time information for the assumed point source. Procedure for the generation of one signal toy MC for time-integrated search and

time-dependent search are mostly the same, with only a difference in Julian data assignment:

1. Assign Julian date:
    - For time-integrated search: the same as the Julian date assignment for background toy MC.
    - For time-dependent search: assign a random value according to the Gaussian distribution of $t_0$ and $\sigma_t$. If this lies in the dead time region (the time between two runs or the time for test runs), we repeat this again.
2. Assign true neutrino energy according to $E_\nu^{-\gamma} \int P(E_\nu, E_\mu^{min}) S(z, E_\nu) dz$.
3. Assign reconstructed muon energy using $f(E_\mu|E_\nu)$.
4. Assign scatter angle $\Delta\phi$ based on $\mathcal{A}(\Delta\phi|E_\mu)$.
5. Calculate the equatorial coordinates.
6. Calculate altitude and azimuth in the detector coordinate.
7. If the event is above horizon, we repeat the steps again.

### 5.4.2 Search Algorithm Confirmation

By running the trials with toy MC, we can check if the algorithm is working properly to find the position and time information of the assumed source. Figure 5.18 and Figure 5.20 are sky maps of $TS$ for time-dependent and time-integrated search, respectively. It is can be seen that the $TS$ distribution for trial with background only toy MC is quite uniform, while those with signals have a $TS_{max}$ located close to the neutrino source position we have set at different declination. In Figure 5.19, we calculated the $TS$ as a function of $t_0$ and $\sigma_t$ for different emission duration.

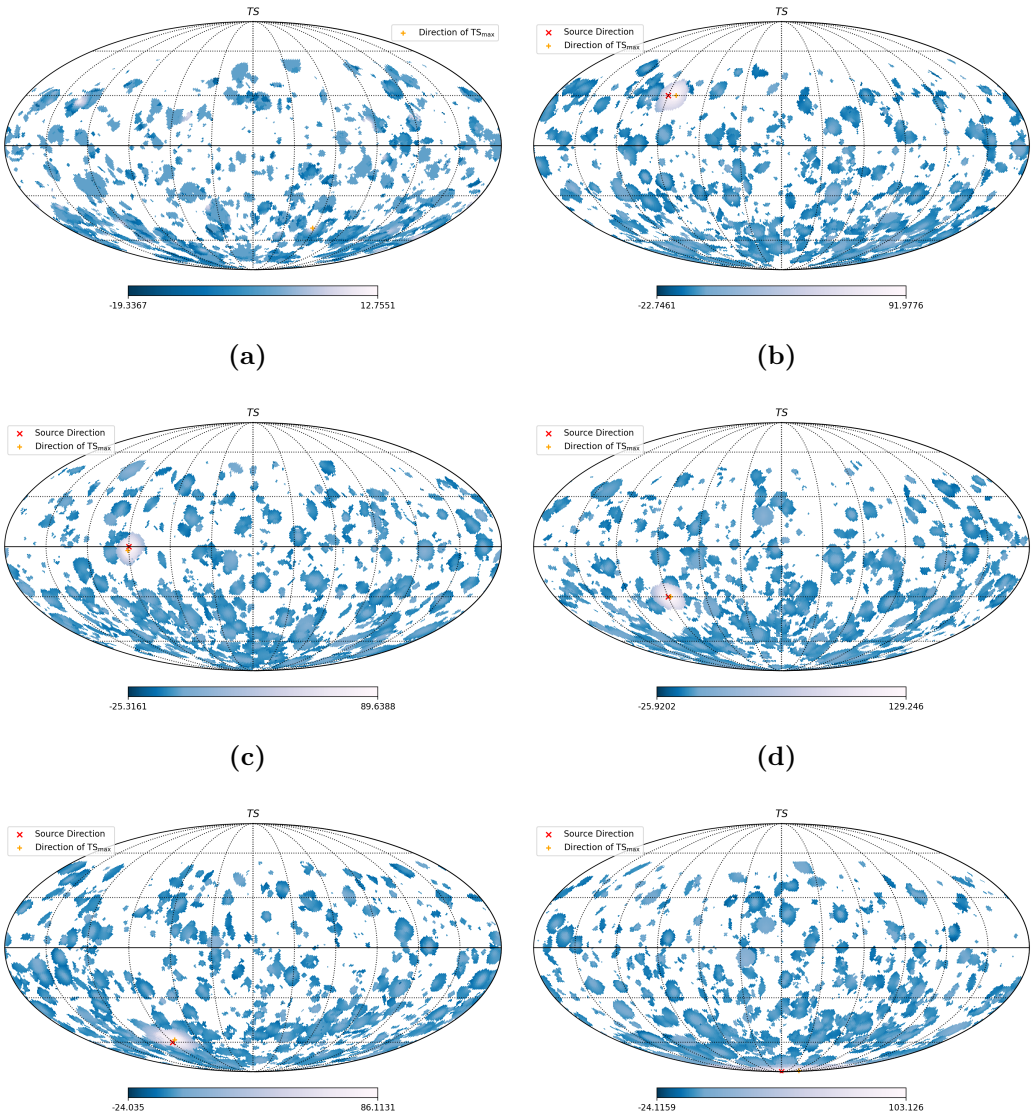


**Figure 5.18:** Sky map of $TS$ of time-dependent search for solely background 5.18a and $n_S = 7$ at $dec = 30°$5.18b, $0°$5.18c, $-30°$5.18d, $-60°$5.18e, $-90°$5.18f. Red cross represents the location of assumed source, and yellow plus represents the direction of $TS_{max}$.

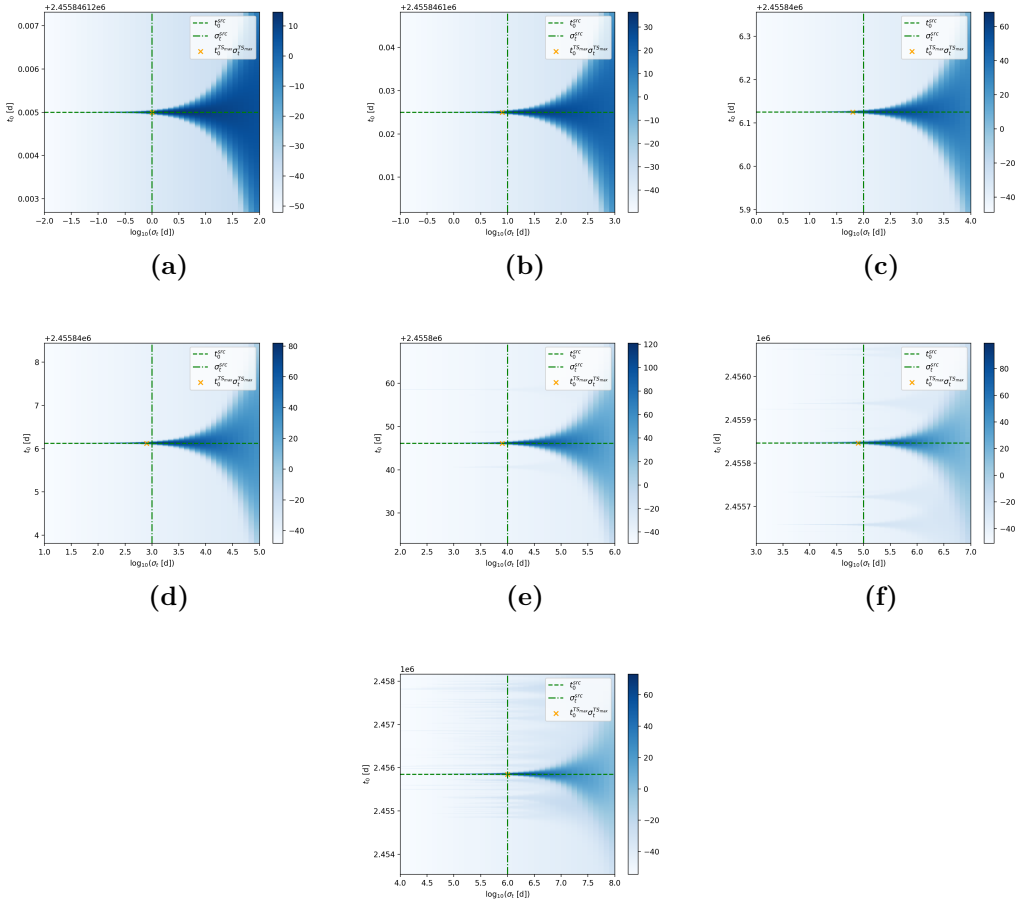

**Figure 5.19:** $TS$ as a function of $t_0$ and $\sigma_t$ for $n_S = 2$ $\sigma_t = 0$s 5.19a, $n_S = 3$ $\sigma_t = 10$s 5.19b, $n_S = 5$ $\sigma_t = 100$s 5.19c, $n_S = 7$ $\sigma_t = 1,000$s 5.19d, $n_S = 10$ $\sigma_t = 10^4$s 5.19e, $n_S = 13$ $\sigma_t = 10^5$s 5.19f, $n_S = 17$ $\sigma_t = 10^6$s 5.19g. Vertical and horizontal dashed green line represents the assumed $\log_{10}\sigma_t$ and $t_0$, respectively. Yellow cross represents the best fitted $\log_{10}\sigma_t$ and $t_0$.

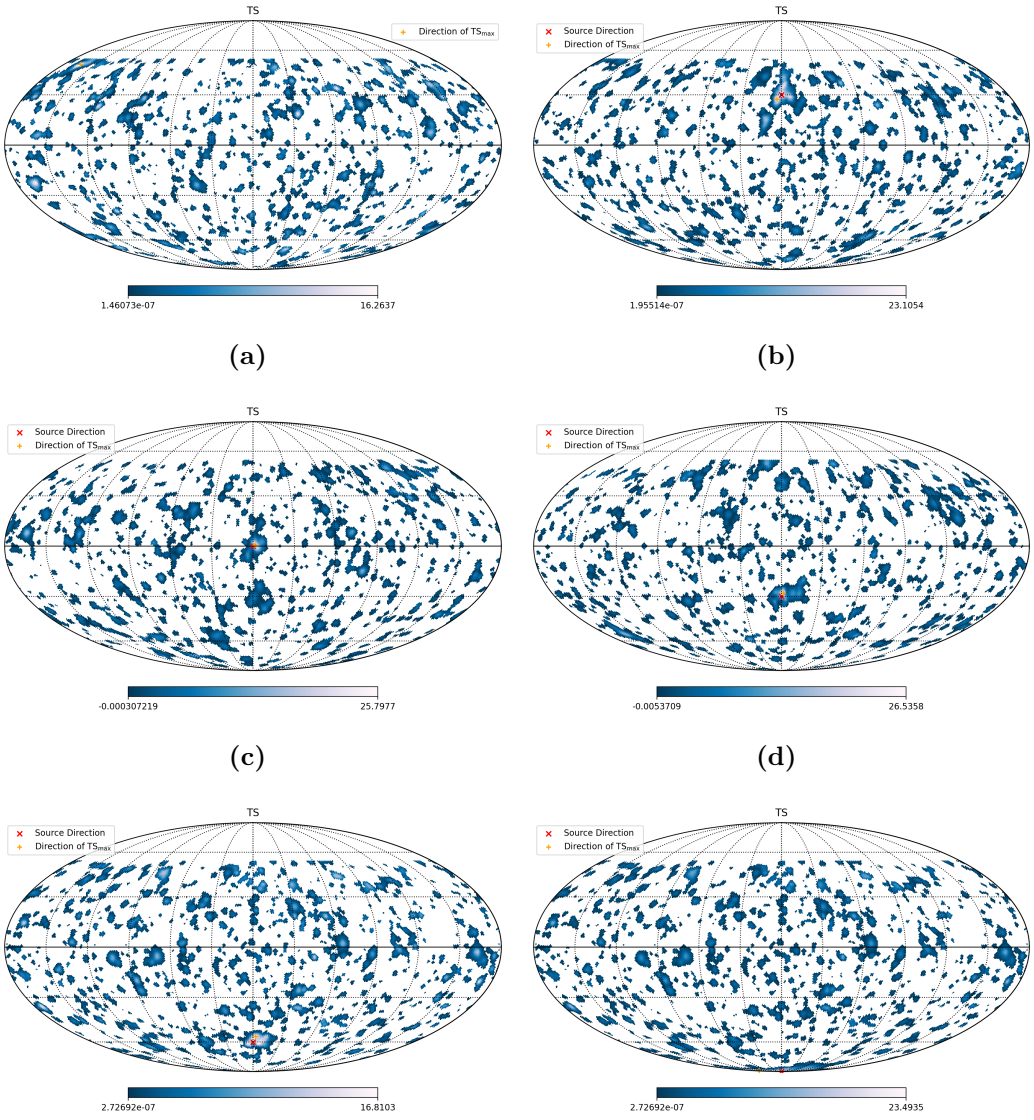


**Figure 5.20:** Sky map of $TS$ of time-integrated search for solely background 5.20a and $n_S = 20$ $dec = 30°$5.20b, $n_S = 20$ $dec = 0°$5.20c, $n_S = 25$ $dec = -30°$5.20d, $n_S = 30$ $dec = -60°$5.20e, $n_S = 40$ $dec = -90°$5.20f. Red cross represents the location of assumed source, and yellow plus represents the direction of $TS_{max}$.

### 5.4.3 Sensitivity

By running many trials for a given $n_S$, we can find the $TS_{max}$ in each trial and get a distribution of $TS_{max}$. Figure5.21 is the $TS_{max}$ distribution for pure backgrounds. The detection threshold is defined the $TS_{max}$ value of 90% CL due to lack of previous detection. We then define the sensitivity as the $n_S$ needed so that 50% of the $TS_{max}$ is larger than the detection threshold. If none of the $n_S$ matches the threshold, we interpolate linearly between two successive values of $n_S$, as shown in Figure5.22.

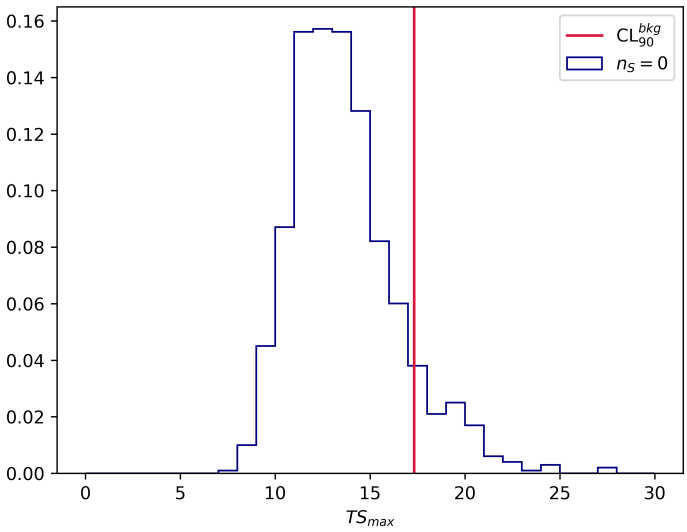


**Figure 5.21:** $TS_{max}$ distribution for solely background events. Vertical red solid line indicates the 90% CL threshold.

Sensitivity for time-integrated search is calculated as a function of the source declination and converted to neutrino fluence using Equation 5.24, as shown in Figure 6.6. And sensitivity for time-dependent search is calculated at different declination and $\sigma_t$, shown in Figure 5.24. Using Equation 5.24, we can convert the sensitivity obtained from Section 5.4.3 into fluence (shown in the right panel of Figure 6.6 and 5.24).

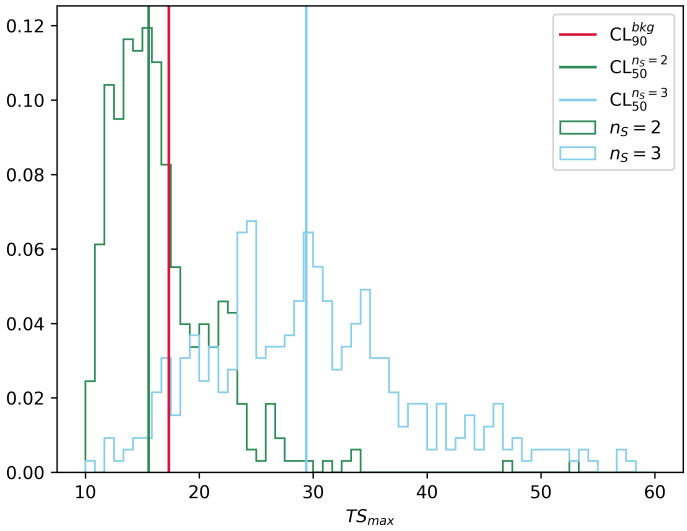


**Figure 5.22:** $TS_{max}$ distribution with different $n_S$. Vertical red solid line indicates the background 90% CL threshold. Vertical blue and green line represent the 50% CL for $n_S = 2$ and $n_S = 3$.

The calculated sensitivity strongly relies on the number of trials we run, especially for the cases where the distribution for two successive $n_S$ values are similar. Such a situation occurs when calculating sensitivity for the time-integrated search at declination above 85°. Running the trials is supper time-consuming, for we only get one $TS_{max}$ value in one trial, but need to perform nearly 50,000 times search in one trial. As a result, we can only provide a less accurate result here.

## 5.5 NEUTRINO FLUENCE

The final results we are interested in is not $n_S$ but neutrino fluence $\Phi(\mathrm{GeVcm}^{-2})$. The relationship between the neutrino fluence and muon fluence is given by:

$$\Phi_\mu = \int_{E_{\nu,max}}^{E_{\nu,max}} dE_\nu \sum_{\nu=\nu_\mu,\bar{\nu}_\mu} P^\nu(E_\nu, E_\mu^{min}) S^\nu(z, E_\nu) \frac{d\Phi_\nu}{dE_\nu} \tag{5.18}$$

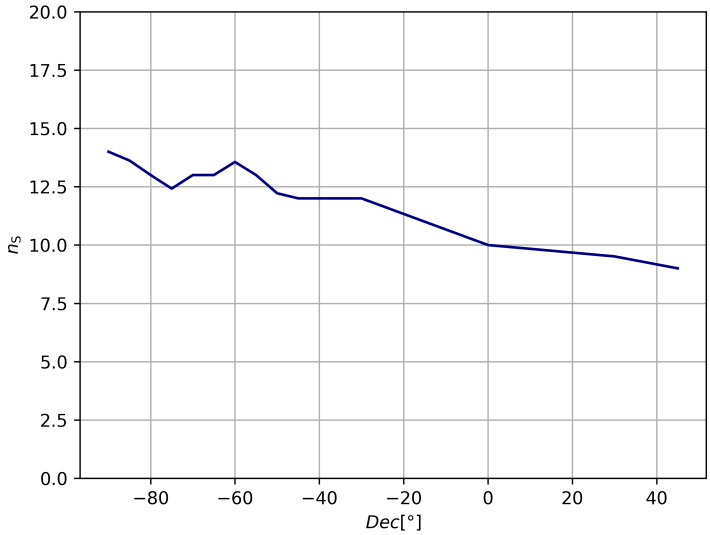


**(a)**

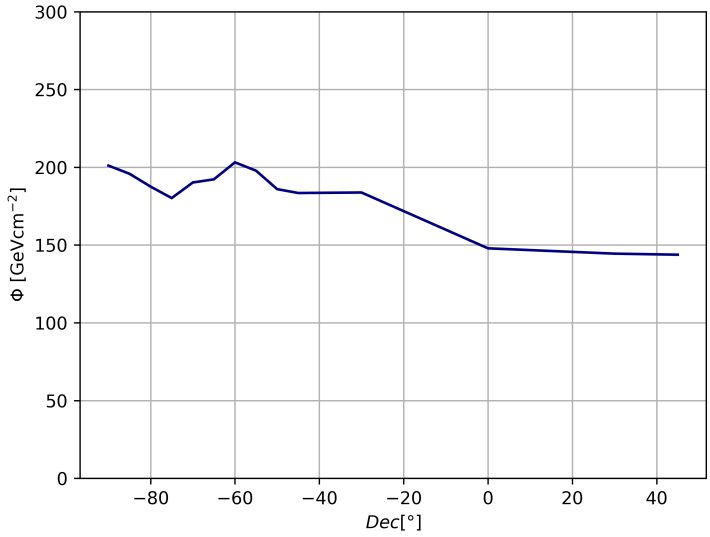


**(b)**

**Figure 5.23:** Sensitivity for time-integrated search in terms of $n_S$ (top) and $\Phi$ (bottom).

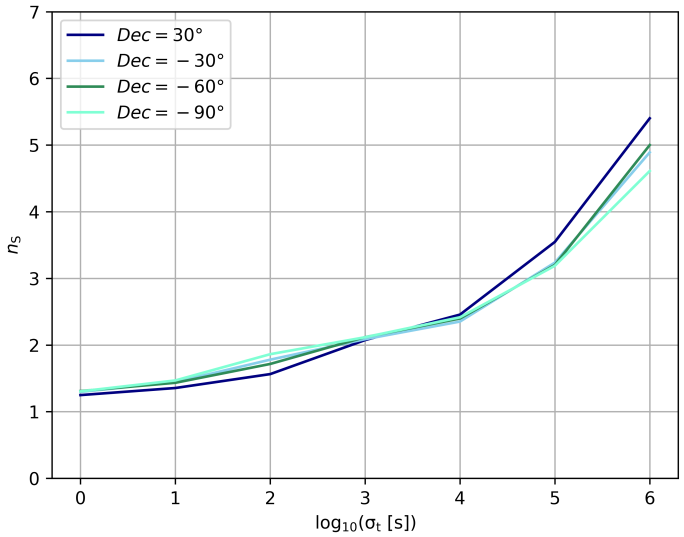


**(a)**

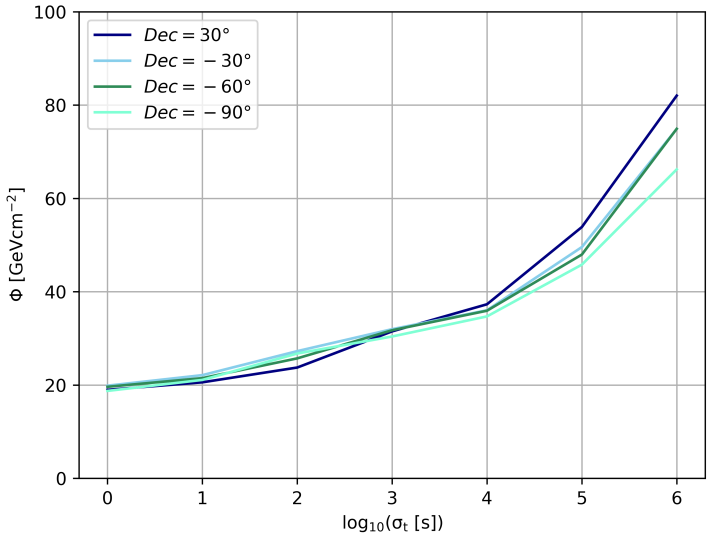


**(b)**

**Figure 5.24:** Sensitivity for time-dependent search in terms of $n_S$ (top) and $\Phi$ (bottom).

By assuming spectrum distribution, we have:

$$\frac{d\Phi_\nu}{dE_\nu} = \Phi_0 E_\nu^{-\gamma} \tag{5.19}$$

and muon fluence can be expressed by:

$$\Phi_\mu = \frac{n_S}{A_{eff}} \tag{5.20}$$

Substitute Equation 5.19 and Equation 5.20 into Equation 5.18, we have:

$$\Phi_0(E_\mu > E_\mu^{min}) = \frac{n_S}{A_{eff}(z)\psi(z)} \tag{5.21}$$

Here

$$\psi(z) = \int_{E_{\nu,max}}^{E_{\nu,max}} dE_\nu \sum_{\nu=\nu_\mu,\bar{\nu}_\mu} P^\nu(E_\nu, E_\mu^{min}) S^\nu(z, E_\nu) E_\nu^{-\gamma} \tag{5.22}$$

is the detection efficiency and $A_{eff}(z)$ is the effective area for SK, $\gamma$ is assumed to be 2 and, $E_{\nu,min} = 1.6$ GeV, $\mathrm{E}_{\nu,\mathrm{max}} = 10^5$ GeV[58].

We have introduced $P^\nu(E_\nu, E_\mu^{min})$ and $S^\nu(z, E_\nu)$ in 5.2.2. With these two parts, we average them with respect to $E_\nu$ together with $\frac{dn_\nu}{dE_\nu}(E_\nu) \propto E_\nu^{-\gamma}$ and get $\psi$ as a function of $z$ (shown in Figure 5.25).

The effective area of SK can be calculated using a numerical technique from [55]:

- Take a large plane next to a cylinder with the same dimensions of SK.
- Construct a grid of 10cm $\times$ 10cm squares on the plane.
- Draw a ray perpendicular to the plane at each grid vertex through the cylinder.
- If the path length inside the cylinder is larger than 7m, the grid is counted as

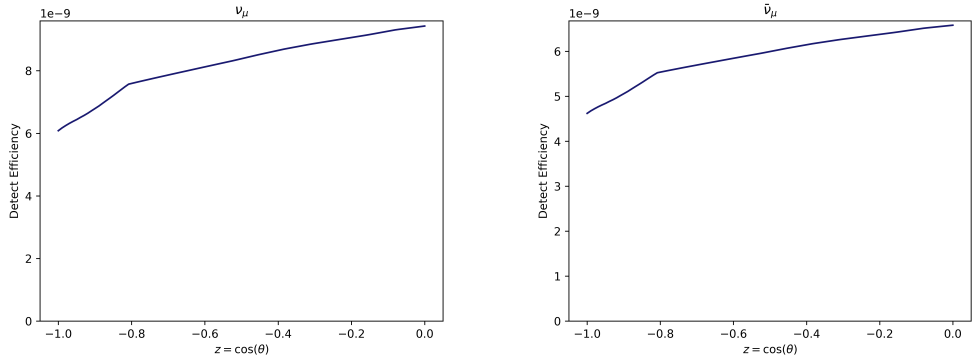


**(a)** **(b)**

**Figure 5.25:** $\psi(z)$ for $\nu_\mu$ (left) and $\bar{\nu}_\mu$ (right)

a part of the effective area contributing 100cm$^2$.

Figure 5.26 is a schematic of how effective area is calculated. This process is repeated

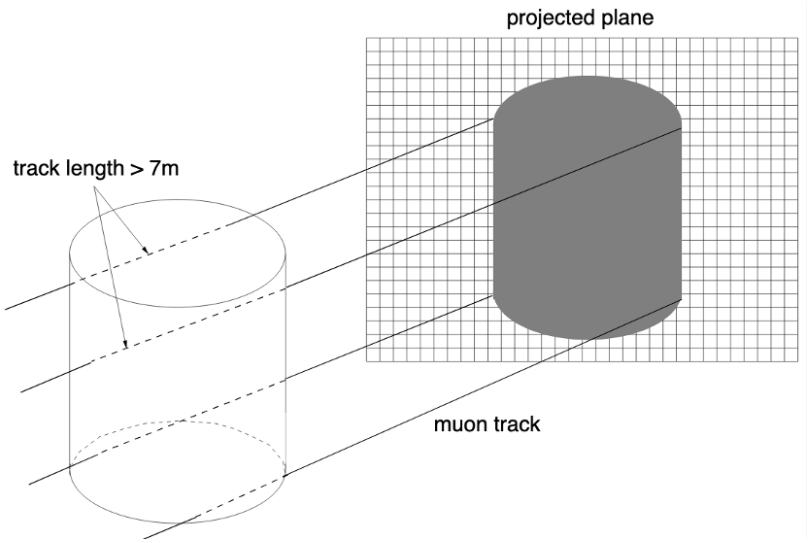


**Figure 5.26:** Schematic of calculating effective area.[55]

for every zenith angle. Then we get the effective area as a function of z, as shown in Figure 5.27

There is one last step we need to do, that is convert these from functions of zenith angle to functions of declination using the relation between zenith angle, declination

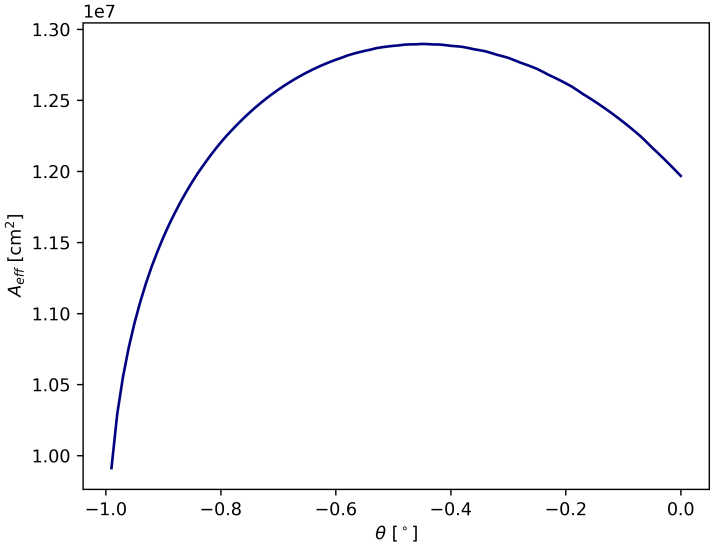


**Figure 5.27:** Effective area as a function of $z$.

and local sidereal time:

$$\psi(dec)A_{eff}(dec) = \frac{\int\limits_{\{t|z(t|dec)<0\}} dt\psi(z)A_{eff}(z)P(t)}{\int\limits_{\{t|z(t|dec)<0\}} dtP(t)} \tag{5.23}$$

Figure 5.28 shows the result of Equation 5.20 This is because the zenith angle is always changing for a certain declination as the Earth is rotating. Then we have:

$$\Phi_0(E_\mu > E_\mu^{min}) = \frac{n_S}{A_{eff}(dec)\psi(dec)} \tag{5.24}$$

$$\tag{5.25}$$

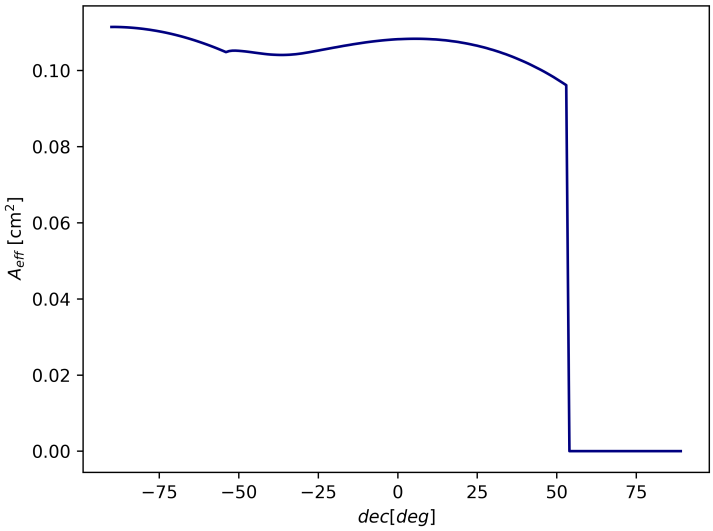


**Figure 5.28:** Product of $\psi(dec)$ and $A_{eff}(dec)$ as a function of declination.

We can also calculate the flux by:

$$\begin{aligned} \varphi &= \Phi_0 \int_{E_{\nu,max}}^{E_{\nu,max}} dE_\nu E_\nu^{-\gamma}/T \\ &= \Phi_0 (E_{\nu,min}^{-\gamma+1} - E_{\nu,max}^{-\gamma})/T \end{aligned} \tag{5.26}$$

For time-integrated search, $T = 2.84 \times 10^8$ s, the total live time of SK-IV.

# CHAPTER 6

## Results and Discussion

## 6.1 RESULTS

### 6.1.1 Time-Integrated Search

$TS$ sky map and histogram of time-integrated search are shown in Figure 6.1 and Figure 6.2. $TS_{max} = 13.32$ occurs at $(198.3°, 15.1°)$. This value is much smaller than the 90%C.L. $TS^{90\%C.L.} = 18.76$, and the post-trial $p$-value is 79.1% (see Figure.6.3). The pre-trial $p$-value is $1.18 \times 10^{-4}$ (Figure 6.4).

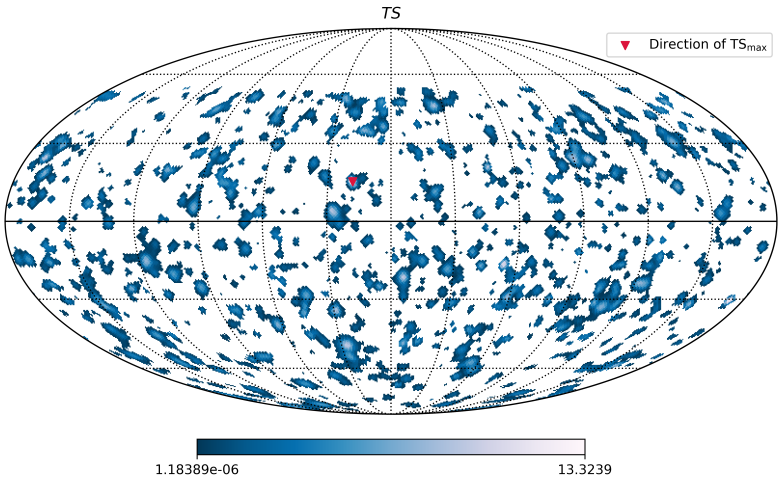


**Figure 6.1:** Sky map of $TS$ for time-integrated search. Location of $TS_{max}$ is marked with red triangle. Positions with $\hat{n}_S = 0$ has been excluded from the sky map, which is represented by the white color region.

Details of the fitted parameters are listed in Table6.1. Figure 6.5 shows a zoomed-in map of the events around $TS_{max}$.

We calculated $\mathcal{L}(n_S|\hat{\gamma})$ as a function of $n_S$ with $\gamma$ fixed at best fitted value $\hat{\gamma}$, and

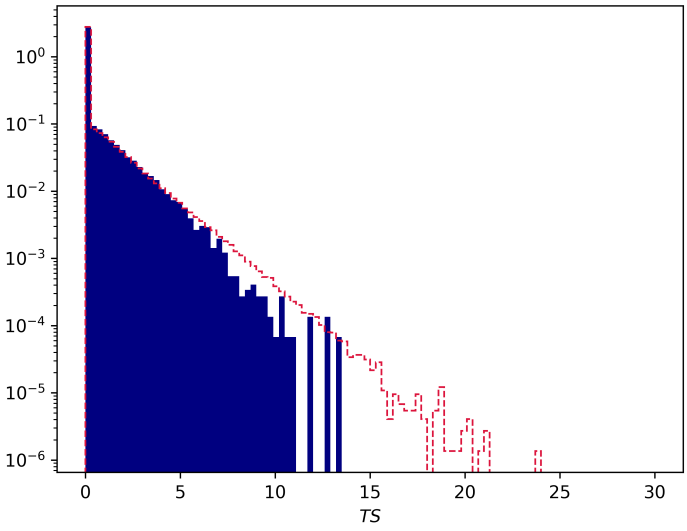


**Figure 6.2:** Blue filled histogram: $TS$ distribution for time-integrated search from all searching directions from data. Red dashed line histogram: $TS$ distribution from all searching directions obtained from 50 trials (roughly 2 million times searches) with solely background toy MC. The peak around 0 represents the situation where $\hat{n}_S = 0$. The result from the data basically agrees with the simulation for background.

**Table 6.1:** Table of the best fitted parameters for time-integrated search.

| $TS$ | $n_S$ | $\gamma$ | $ra$ [°] | $dec$ [°] | pre-trial $p$ | post-trial $p$ |
|---|---|---|---|---|---|---|
| 13.32 | 7.913 | 2.58 | 198.3 | 15.1 | $1.18 \times 10^{-4}$ | 79.1% |

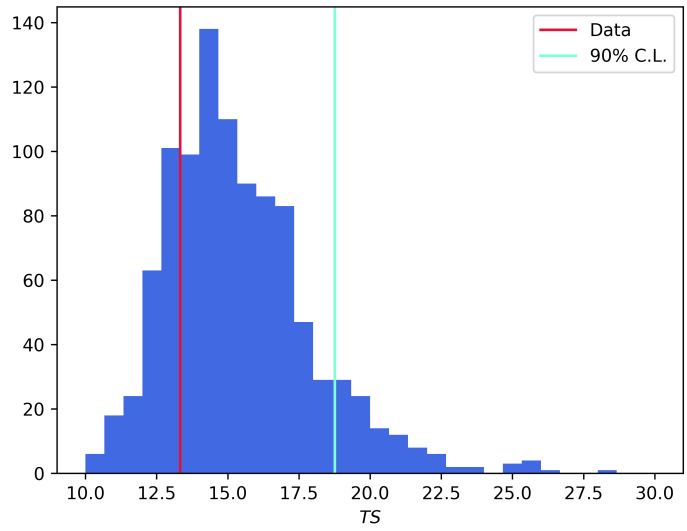


**Figure 6.3:** The histogram of post-trial $TS_{max}$ distribution for time-integrated search obtained from 1,000 trials with solely background toy MC.

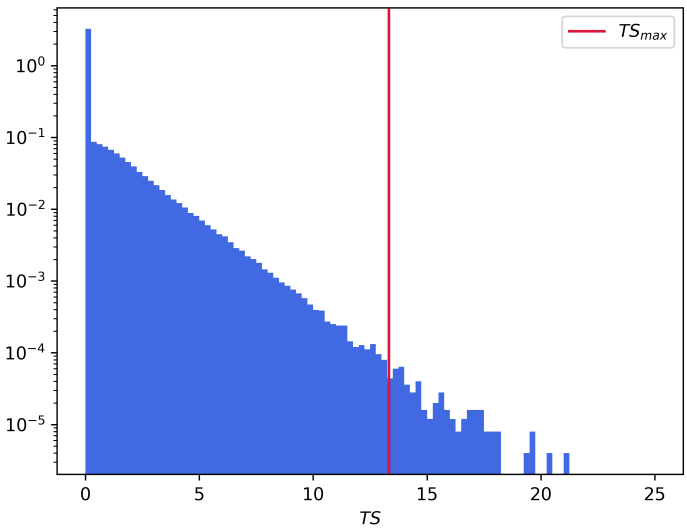


**Figure 6.4:** Histogram of pre-trial $TS$ distribution for time-integrated search by simulating $10^6$ times at the position of $TS_{max}$.

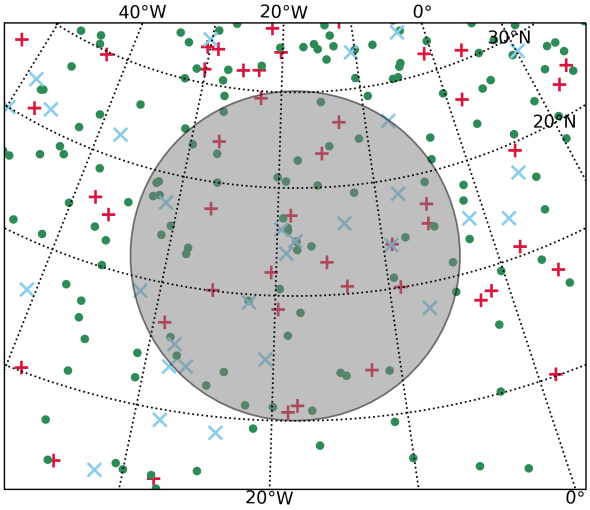


**Figure 6.5:** Stopping (red plus), through-going (green dot) and showering (blue cross) UPMU events detected around the position of $TS_{max}$. Grey region encircled by the black circle is the 15° search cone.

calculated upper limit by

$$90\% = \frac{\int_0^{n_S^{upper}} dn_S \mathcal{L}(n_S, ...)}{\int_{-\infty}^{+\infty} dn_S \mathcal{L}(n_S, ...)} \tag{6.1}$$

The result $n_S^{upper} = 13.86$, with corresponding fluence upper limit $\Phi_0^{upper} = 2.06 \times 10^2$ GeVcm$^{-2}$ and flux upper limit $\varphi^{upper} = 4.53 \times 10^{-7}$ cm$^{-2}$s$^{-1}$:

### 6.1.2 Time-Dependent Search

Figure6.7 and Figure 6.8 show the sky map and histogram of $TS$. The maximum $TS$ occurs at $(118.0°, -62.7°)$, with $TS_{max} = 14.53$. This value is smaller than the the threshold $TS^{90\%C.L.} = 17.8$. The post-trial $p$-value is 33.4%, with the pre-trial $p$-value found to be $2.24 \times 10^{-4}$, as shown in Figure 6.9 and Figure6.10. The best fitted time of the emission is 13:09:42 JST, October 27$^{th}$, 2010, with a emission duration $(2\hat{\sigma}_t)$

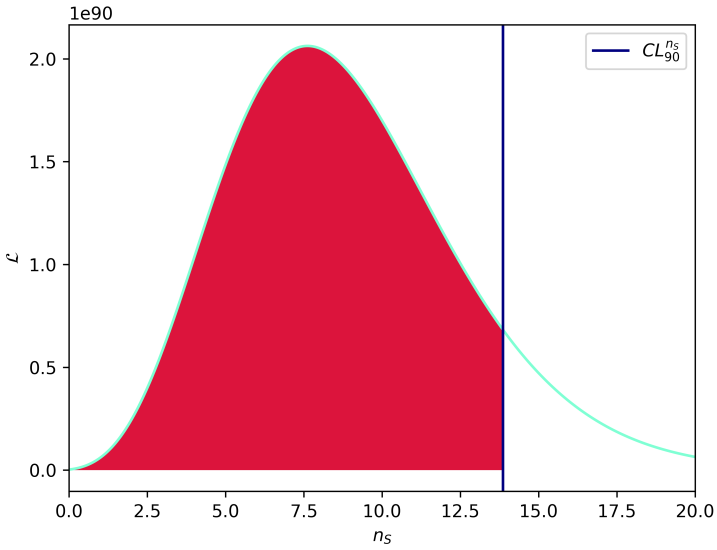


**Figure 6.6:** $\mathcal{L}(n_S|\hat{\gamma})$ as a function of $n_S$ with $\gamma$ fixed to the best fitted value $\hat{\gamma}$. The vertical solid blue line represent the upper limit for 90% CL.

of around 5.1 hours. Rest of the best fitted parameters of the top three $TS$ are listed in Table 6.2.

**Table 6.2:** Table of the best fitted parameters of the top three largest $TS$ for time-integrated search.

| $TS$ | $n_S$ | $\gamma$ | $t_0$[mjd] | $\sigma_t$[s] | $ra$ [°] | $dec$ [°] | pre $p$ | post $p$ |
|---|---|---|---|---|---|---|---|---|
| 14.53 | 1.996 | 1.56 | 2010.10.27 04:04:48 | $9.25 \times 10^3$ | 118.0 | -62.7 | $2.24 \times 10^{-4}$ | 33.4% |
| 13.96 | 1.999 | 2.50 | 2009.09.27 03:07:12 | $3.37 \times 10^3$ | 3.4 | 12.0 | $5.08 \times 10^{-5}$ | 39.5% |
| 12.07 | 3.829 | 3.00 | 2016.03.03 21:24:30 | $1.36 \times 10^5$ | 277.9 | -60.2 | $6.09 \times 10^{-4}$ | 69.2% |

Since no excess was found with respect to the background, we calculate the upper limit of the neutrino flux. In Figure 6.11, we calculated the $\mathcal{L}(n_S|\hat{\gamma}, \hat{t}_0, \hat{\sigma}_t)$ as a function of $n_S$ at the position where $TS_{max}$ occurs. The results are $n_S^{upper} = 5.29$, with corresponding $\Phi_0^{upper} = 78.6$ GeVcm$^{-2}$ for the $1^{st}$ largest $TS$, $n_S^{upper} = 5.27$, with corresponding $\Phi_0^{upper} = 78.1$ GeVcm$^{-2}$ for the $2^{nd}$ largest $TS$ and $n_S^{upper} = 7.84$, with corresponding $\Phi_0^{upper} = 117.3$ GeVcm$^{-2}$ for the $3^{rd}$ largest $TS$. The emission time

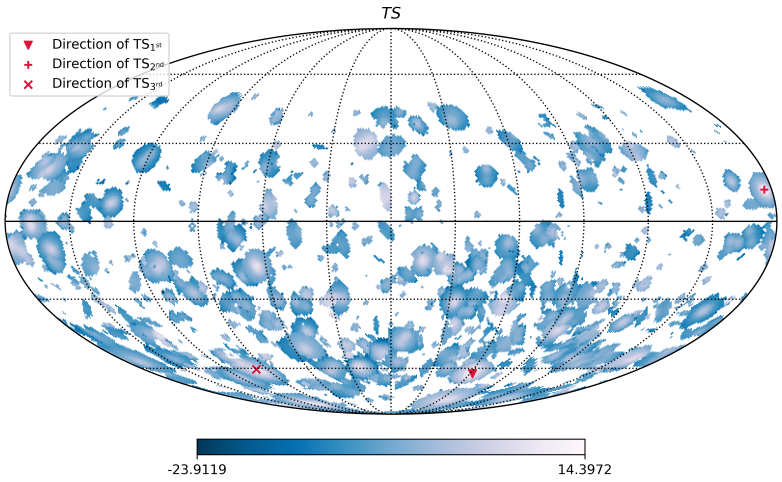


**Figure 6.7:** Sky map of $TS$ for time-dependent search. The locations of the top three maximum $TS$s are marked with red triangle, plus and cross, respectively. Positions with $\hat{n}_S = 0$ has been excluded from the sky map, which is represented by the white color region.

interval is estimated by $2\hat{\sigma}_t$ ($1.85 \times 10^4$ s, $6.74 \times 10^4$ s and $2.72 \times 10^5$ s for $1^{st}$, $2^{nd}$ and $3^{rd}$, respectively).

It is clear that most of the events are more background-like, but we do find something interesting at the largest three $TS$. At least two events with offset less than $5^\circ$ from the fitted source direction in a time region of $\pm\hat{\sigma}_t$ are found at each of these three positions. The information of are listed in Table 6.3. Figure 6.12 shows the orientation of the events with their angular uncertainties and their time information.

## 6.2 POTENTIAL CANDIDATE CHECK

After obtaining all the results, we tried to find potential sources which is coincident with the largest three $TS$. The first candidate is the TXS 0506+56 discussed in Chapter 1, but none of these three matches either with direction $(77.36^\circ, 5.69^\circ)$ or

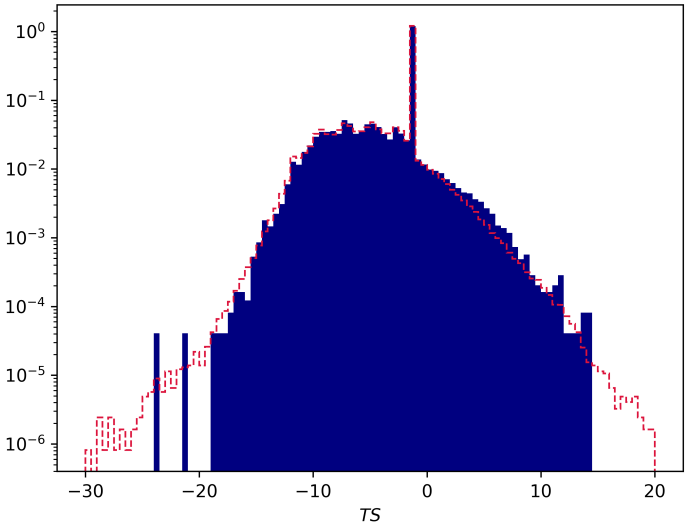


**Figure 6.8:** Blue filled histogram: $TS$ distribution for time-integrated search from all searching directions from data. Red dashed line histogram: $TS$ distribution from all searching directions obtained from 50 trials with solely background toy MC. The peak around 0 represents the situations where $\hat{n}_S = 0$ and $\hat{\sigma}_t = (T_{end} - T_{start})/2$, the maximum value set for $\sigma_t$. The result from the data basically agrees with the simulation for background.

**Table 6.3:** Energy, distance from best fitted position, time interval from the best fitted $t_0$, and event type of the events within 15° to the position of the top three largest $TS$ with in $7\hat{\sigma}_t$ around $\hat{t}_0$.

| | $E_i$[GeV] | $\Delta\phi$ [°] | $\Delta t$ [$s$] | Event Type |
|---|---|---|---|---|
| $1^{st}$ | 10.26 | 1.18 | $-8.64 \times 10^3$ | Through |
| | 37.74 | 1.90 | $9.50 \times 10^3$ | Showering |
| $2^{nd}$ | 7.04 | 1.26 | $-3.46 \times 10^3$ | Through |
| | 9.29 | 0.57 | $2.59 \times 10^3$ | Through |
| $3^{rd}$ | 0.78 | 5.90 | $-2.37 \times 10^5$ | Through |
| | 8.99 | 11.01 | $-1.37 \times 10^5$ | Showering |
| | 2.67 | 2.99 | $2.25 \times 10^4$ | Stop |
| | 9.66 | 1.18 | $2.94 \times 10^4$ | Showering |
| | 4.45 | 5.26 | $1.52 \times 10^5$ | Stop |

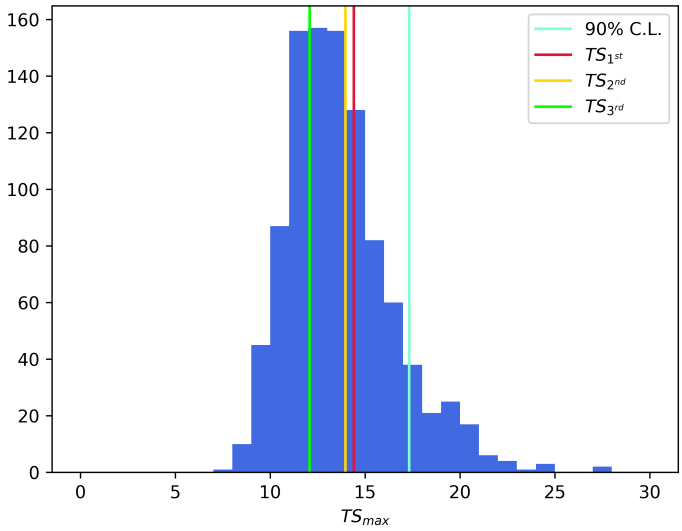


**Figure 6.9:** The histogram of post-trial $TS_{max}$ distribution for time-dependent search obtained from 1,000 trials with solely background toy MC.

time (2017.09.22). Then we compared the alerts of high-energy neutrino in IceCube catalogue[2] and 27 potential candidates taken from [21], as shown in Figure 6.13, Table 6.4 and Table 6.5, and still found no match. Finally, we checked the catalogs and astronomical archives of HEASARC[1].

## 6.3 DISCUSSION

In comparison with the previous time-integrated search for astrophysical neutrino point sources from SK-I to SK-III in [58], this search additionally included the energy distribution in the likelihood to consider different power-law emission spectra with varying spectral index. The sensitivity $3.63 \times 10^{-7}$ [$\mathrm{cm}^{-2}\mathrm{s}^{-1}$ averaged in the declination region $(-30°, 0°)$ is comparable to $3 \times 10^{-7}$ $\mathrm{cm}^{-2}\mathrm{s}^{-1}$ in previous search. There is no events or celestial objects that has an obvious coincidence with the position or time of the largest $TS$ in either time-integrated search and time-dependent

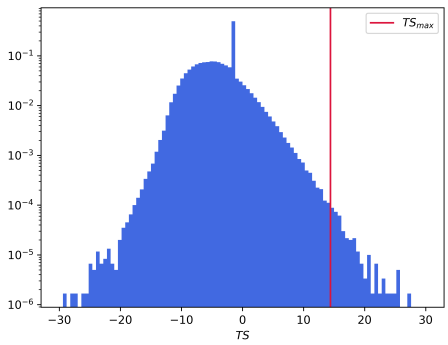


**(a)**

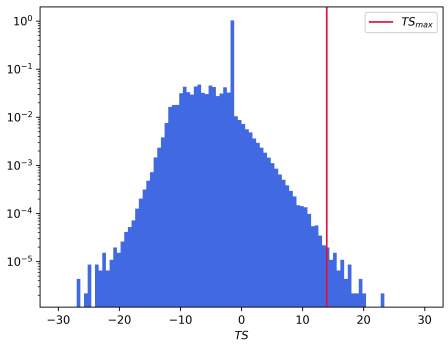


**(b)**

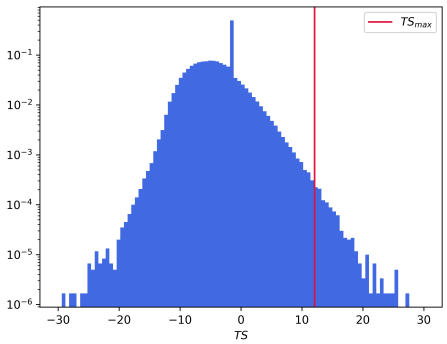


**(c)**

**Figure 6.10:** Histograms of pre-trial $TS$ distribution for time-dependent search of $1^{st}$ (top), $2^{nd}$ (middle) and $3^{rd}$ (bottom). Each one is simulated $10^6$ times at the corresponding direction.

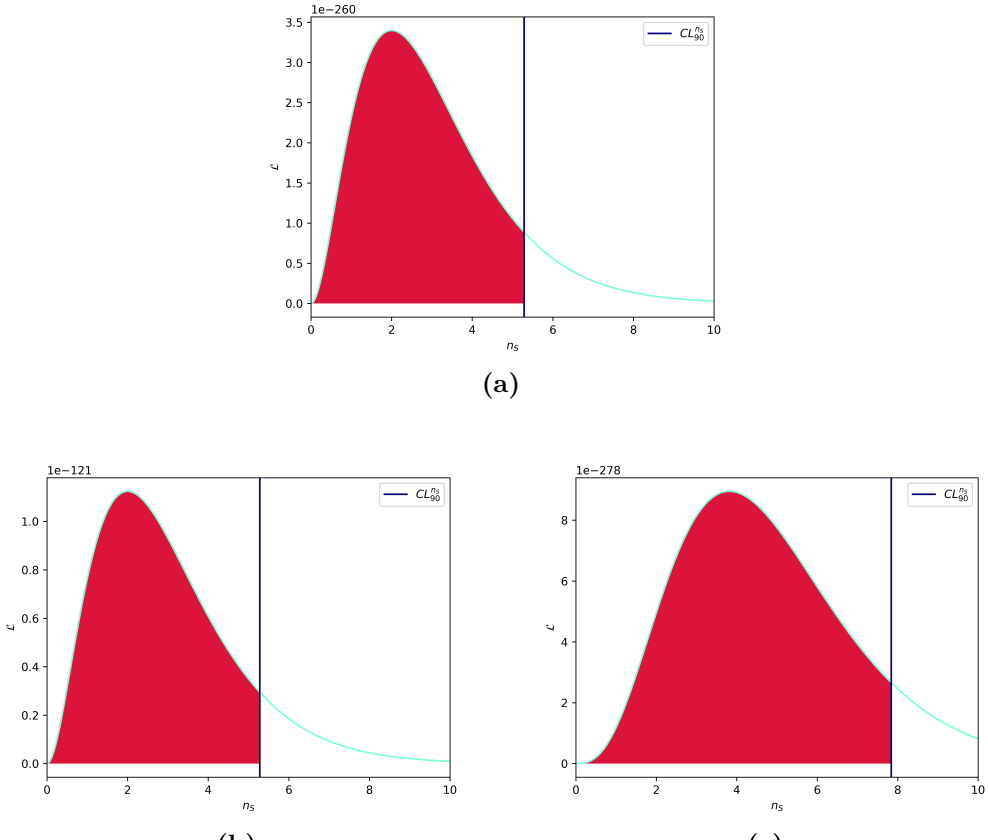


**Figure 6.11:** $\mathcal{L}(n_S|\hat{\gamma}, \hat{t}_0, \hat{\sigma}_t)$ as a function of $n_S$ with $\gamma$, $t_0$ and $\sigma_t$ fixed to the best fitted value $\hat{\gamma}$, $\hat{t}_0$ and $\hat{\sigma}_t$, for $1^{st}$ (top), $2^{nd}$ (middle) and $3^{rd}$ (bottom). The vertical line represents the upper limit for 90% CL.

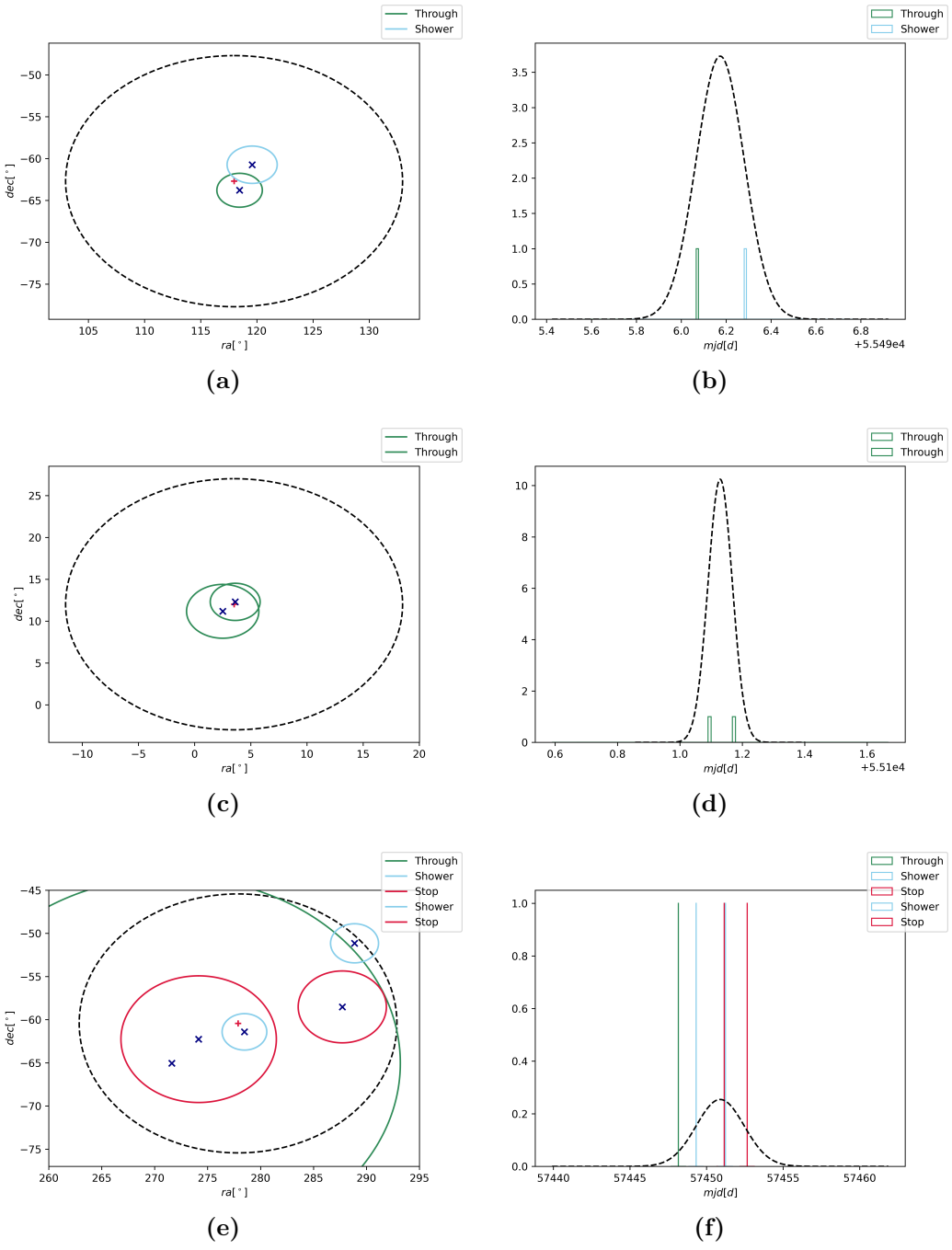


**Figure 6.12:** Space orientation (left column) and time distribution (right column) of the events within 15° to the position of the $1^{st}$ (top), $2^{nd}$ (middle) and $3^{rd}$ (bottom) largest $TS$ with in $7\hat{\sigma}_t$ around $\hat{t}_0$. Black dashed circle in the left figures is the boundary of the search cone. The red plus indicates the best fitted source position. Blue cross is the direction of the UPMU event, with the circle around them being the angular resolution. The black dashed line in the right figures is the Gaussian distribution with the best fitted $t_0$ and $\sigma_t$ as the parameter.

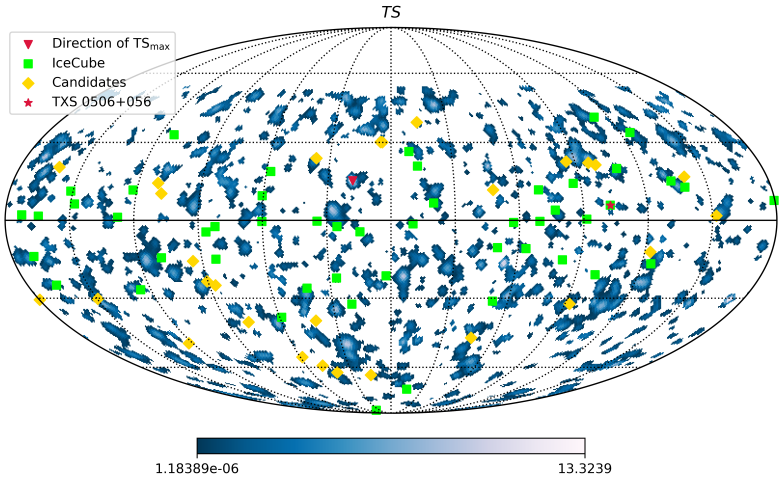


**(a)**

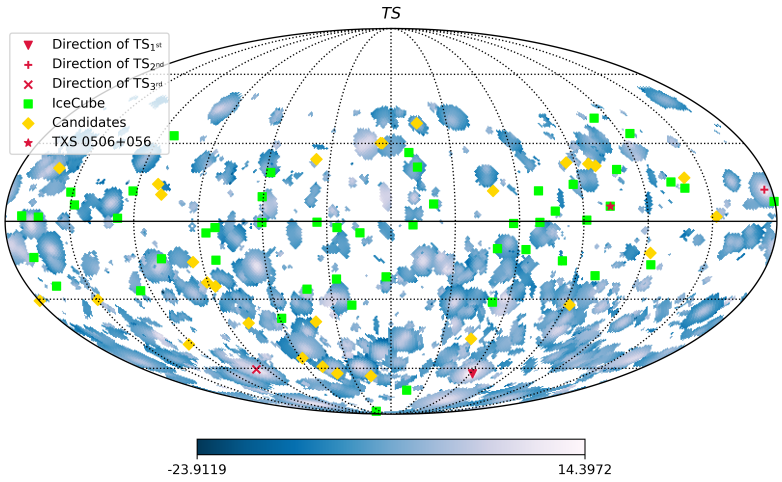


**(b)**

**Figure 6.13:** $TS$ sky map for time-integrated (top) and time-dependent (bottom) search, with the the green squares represent the events from IceCube alert catalog (Table 6.4) and yellow diamonds represent the candidates from list in Table 6.5, and the red dot is the location of TXS 0506+056.

**Table 6.4:** List of the IceCube alert.

| UTC | ra [°] | dec [°] | UTC | ra [°] | dec [°] |
|---|---|---|---|---|---|
| 2010-09-12 01:41:53 | 127.9 | -31.2 | 2010-11-12 13:14:21 | 110.56 | -0.37 |
| 2011-02-16 19:40:59 | 182.4 | -21.2 | 2011-07-14 02:42:41 | 67.86 | 40.32 |
| 2011-12-28 12:45:49 | 345.6 | -24.8 | 2012-05-01 13:41:24 | 164.8 | -71.5 |
| 2013-04-08 04:31:49 | 167.17 | 20.67 | 2013-06-27 02:38:57 | 93.43 | 14.02 |
| 2013-12-02 13:39:09 | 206.63 | -22.02 | 2014-01-22 04:54:26 | 219.64 | -86.16 |
| 2014-04-20 01:35:28 | 238.98 | -37.73 | 2014-11-09 04:58:36 | 55.63 | -16.50 |
| 2014-12-09 03:26:05 | 160.05 | 6.57 | 2015-04-28 11:20:46 | 80.77 | -20.75 |
| 2015-09-11 13:34:02 | 240.20 | -0.45 | 2015-12-07 10:36:57 | 0.4 | 7.5 |
| 2016-04-27 05:52:32 | 240.57 | 9.34 | 2016-08-14 21:45:54 | 200.3 | -32.4 |
| 2016-11-03 09:07:31 | 40.83 | 12.56 | 2017-03-12 13:49:39 | 305.15 | -26.61 |
| 2017-05-06 12:36:56 | 221.8 | -26.0 | 2010-10-09 09:08:02 | 331.09 | 11.10 |
| 2010-10-28 07:16:47 | 88.68 | 0.46 | 2011-01-28 01:30:24 | 307.53 | 1.19 |
| 2011-03-04 22:54:57 | 116.37 | -10.72 | 2011-09-30 10:41:00 | 266.48 | -4.41 |
| 2012-03-01 19:21:57 | 238.01 | 18.60 | 2012-05-23 13:46:58 | 171.03 | 26.36 |
| 2012-09-22 13:11:01 | 70.75 | 19.79 | 2012-10-11 18:30:09 | 205.22 | -2.39 |
| 2013-09-07 19:02:03 | 129.81 | -10.36 | 2013-10-23 13:24:14 | 301.82 | 11.49 |
| 2013-12-04 11:16:53 | 289.16 | -14.25 | 2014-01-08 07:23:22 | 344.53 | 1.57 |
| 2014-01-09 12:04:17 | 292.85 | 33.06 | 2014-02-03 18:50:34 | 349.54 | -13.71 |
| 2014-06-10 16:54:23 | 110.30 | 11.57 | 2014-09-23 17:18:22 | 169.72 | -1.34 |
| 2015-08-12 18:13:05 | 328.19 | 6.21 | 2015-08-31 05:13:40 | 54.85 | 33.96 |
| 2015-09-23 00:38:35 | 103.27 | 3.88 | 2015-09-26 21:37:43 | 194.50 | -4.34 |
| 2015-11-22 12:45:31 | 262.18 | -2.38 | 2016-01-28 04:24:11 | 263.40 | -14.79 |
| 2016-05-10 15:56:05 | 352.34 | 2.09 | 2016-07-31 01:55:03 | 214.5 | -0.33 |
| 2016-08-06 12:21:33 | 122.81 | -0.81 | 2016-12-10 20:06:41 | 46.58 | 14.98 |
| 2017-03-21 07:32:21 | 98.30 | -15.02 | 2017-09-22 20:54:30 | 77.43 | 5.72 |

**Table 6.5:** List of potential astrophysical neutrino source candidates[21]. The column from left is name, declination, right ascension, distance measured in z (redshift) or kpc, observed gamma ray flux, energy threshold for flux integration, gamma ray emission energy spectrum index[60], and neutrino flux 90 CL upper limit at that direction for time-integrated search (averaged for total live time of SK-IV).

| Name | dec [°] | ra [°] | distance | $\Phi_\gamma$ [$\times 10^{-12}$cm$^{-2}$s$^{-1}$] | $E_{th}$ [TeV] | $\gamma$ | $\Phi_\nu^{90\mathrm{CL}}$[$\times 10^{-7}$cm$^{-2}$s$^{-1}$] |
|---|---|---|---|---|---|---|---|
| 1ES0347-121 | -11.99 | 57.35 | z=0.19 | 3.9[18] | 0.25 | 3.1 | 1.36 |
| RBS0723 | 11.56 | 131.80 | z=0.20 | 2.6[14] | 0.2 | 3.6 | 1.39 |
| H2356-309 | -30.63 | 359.78 | z=0.17 | 4.1[17] | 0.2 | 3.1 | 1.07 |
| PKS2005-489 | -48.82 | 302.37 | z=0.07 | 2.6[15] | 0.4 | 3.2 | 1.09 |
| PKS0548-322 | -32.27 | 87.67 | z=0.07 | 2.7[16] | 0.25 | 2.9 | 2.15 |
| RGBJ0152+017 | 1.79 | 28.17 | z=0.08 | 2.7[19] | 0.3 | 3.0 | 1.43 |
| RGBJ2243+203 | 20.35 | 340.98 | - | 78[10] | 0.112 | 4.6 | 1.42 |
| VERJ0521+211 | 21.21 | 80.44 | - | 19[23] | 0.2 | 3.4 | 2.19 |
| PKS1440-389 | -39.14 | 220.99 | z=0.14 | 19[7] | 0.147 | 3.7 | 1.12 |
| 1ES1215+303 | 30.10 | 184.45 | z=0.13 | 8.0[22] | 0.2 | 3.6 | 3.03 |
| PKS1424+240 | 23.79 | 216.75 | - | 21[24] | 0.12 | 3.8 | 1.40 |
| PKS2155-304 | -30.22 | 329.72 | z=0.12 | 43[11] | 0.2 | 3.5 | 1.96 |
| Markarian421 | 38.19 | 166.08 | z=0.03 | 310[20] | 0.4 | 2.2 | 3.21 |
| 1ES1218+304 | 30.19 | 185.36 | z=0.18 | 12[13] | 0.2 | 3.1 | 3.11 |
| PSRB1259-63 | -63.83 | 195.70 | 2.7 kpc | 0.4[6] | 1 | 2.6 | 2.48 |
| Terzan5 | -24.90 | 266.95 | 5.9 kpc | 0.3[6] | 1 | 2.4 | 1.72 |
| Crab | 22.01 | 83.63 | 2.0 kpc | 21[40] | 1 | 2.5 | 3.28 |
| RCW86 | -62.48 | 220.68 | 2.5 kpc | 2.4[6] | 1 | 1.6 | 1.58 |
| MSH15-52 | -59.16 | 228.53 | 5.2 kpc | 5.7[6] | 1 | 2.3 | 1.04 |
| SNRG327.1-01.1 | -55.08 | 238.65 | 9.0 kpc | 0.29[6] | 1 | 2.2 | 1.13 |
| RXJ0852.0-4622 | -46.37 | 133.00 | 0.2 kpc | 23[6] | 1 | 1.8 | 2.24 |
| RXJ1713.7-3946 | -39.75 | 258.25 | 1.0 kpc | 17[6] | 1 | 2.1 | 1.34 |
| W28 | -23.34 | 270.43 | 2.0 kpc | 0.45[6] | 1 | 2.7 | 1.54 |
| SNRG015.4+00.1 | -15.47 | 274.52 | 4.8 kpc | 0.23[6] | 1 | 2.1 | 0.95 |
| HESSJ1912+101 | 10.15 | 288.21 | - | 2.5[6] | 1 | 2.7 | 1.02 |
| W51C | 14.19 | 290.75 | 5.4 kpc | 0.69[6] | 1 | 2.6 | 1.29 |
| IC443 | 22.50 | 94.21 | 1.5 kpc | 4.6[12] | 0.3 | 3.0 | 1.58 |

search. For the direction of the second largest in time-dependent search, the closest event both in space and in time is a GRB numbered as GRB090428552 detected $157.9'$ away (at $(0.8°, 11.5°)$) and about 5 month earlier (on 2009.04.28). The GRB typically last from several seconds to several thousand seconds, and no evidence has suggested that the neutrino emission from the GRB has a time delay compared with gamma ray emission up to several month, so we just keep this as a record for future study. As for the third one, a known pulsar PSR J1833-6023 is located within 18.5' away from it at $(278.3°, -60.4°)$. It is possible that these are related, but further study regarding this is needed to confirm it.

# CHAPTER 7

## Summary and Prospects

In this study, we performed both time-integrated search and time-dependent search in the full sky for high-energy (above 1.6 GeV) astrophysical neutrino point sources in SK-IV with UPMU. Unfortunately, no excess with respect to the background is found in either search.

The most significant cluster in the full sky for the time-integrated search is at $(198.3^\circ, 15.1^\circ)$ in J2000 equatorial coordinate system with pre-trial $p$-value of $1.18 \times 10^{-4}$ and post-trial $p$-value of 79.2% . The upper limit of the neutrino fluence is $\Phi_0 = 2.06 \times 10^2$ [GeVcm$^{-2}$] and corresponding flux is $\varphi^{upper} = 4.53 \times 10^{-7}$ cm$^{-2}$s$^{-1}$.

For the time-dependent search, the most significant cluster is at $(118.0^\circ, -62.7^\circ)$ on 2010.10.27 13:09:42 JST and $\hat{\sigma}_t = 9.25 \times 10^3$ s. The pre-trial $p$-value is $2.24 \times 10^{-4}$ and post-trial $p$-value is 33.4%. Neutrino fluence upper limit is set to $\Phi_0 = 7.86 \times 10^1$ [GeVcm$^{-2}$], with the emission time interval estimated by $1.85 \times 10^4$ s ($2\hat{\sigma}_t$).

There are still a lot of work that could be done which is related to this study. Although not many, part of the FC and PC data still have a good-enough angular resolution which could be used for the search. And till now the SK-V data is completely ready and a joint search from SK-I to SK-V can be performed. Except for the full sky search, trigger based search could also help to reduce the huge trial factor raised when looking for too many directions at a time.

In addition to the present experiment facility, the next-generation neutrino detector Hyper-Kamiokande (HK) has already been constructed. With larger water tank and more PMTs, we can expect a better detection performance in the future.

# BIBLIOGRAPHY


[1] Nasa's heasarc: Archive. https://heasarc.gsfc.nasa.gov/docs/archive.html.

[2] Icecube catalog of alert events up through icecube-170922a. https : / / icecube . wisc . edu / data-releases / 2018 / 07 / icecube-catalog-of-alert-events-up-through-icecube-170922a/, 2018.

[3] Healpix. https://healpix.sourceforge.io/, 2019.

[4] M. Aartsen, M. Ackermann, J. Adams, J. Aguilar, M. Ahlers, M. Ahrens, D. Altmann, T. Anderson, M. Archinger, C. Arguelles, et al. Searches for time-dependent neutrino sources with icecube data from 2008 to 2012. *The Astrophysical Journal*, 807(1):46, 2015.

[5] R. Abbasi, M. Ackermann, J. Adams, J. Aguilar, M. Ahlers, M. Ahrens, C. Alispach, A. Alves, N. Amin, K. Andeen, et al. A search for time-dependent astrophysical neutrino emission with icecube data from 2012 to 2017. *The Astrophysical Journal*, 911(1):67, 2021.

[6] H. Abdalla, A. Abramowski, F. Aharonian, F. A. Benkhali, E. Angüner, M. Arakawa, M. Arrieta, P. Aubert, M. Backes, A. Balzer, et al. The hess galactic plane survey. *Astronomy & Astrophysics*, 612:A1, 2018.

[7] H. Abdalla, R. Adam, F. Aharonian, F. Ait Benkhali, E. Angüner, M. Arakawa, C. Arcaro, C. Armand, T. Armstrong, H. Ashkar, et al. Very high energy $\gamma$-ray emission from two blazars of unknown redshift and upper limits on their distance. *Monthly Notices of the Royal Astronomical Society*, 494(4):5590–5602, 2020.

[8] K. Abe, C. Bronner, Y. Haga, Y. Hayato, M. Ikeda, K. Iyogi, J. Kameda, Y. Kato, Y. Kishimoto, L. Marti, et al. Atmospheric neutrino oscillation analysis with external constraints in super-kamiokande i-iv. *Physical Review D*, 97(7):072001, 2018.

[9] K. Abe, C. Bronner, G. Pronost, Y. Hayato, M. Ikeda, K. Iyogi, J. Kameda, Y. Kato, Y. Kishimoto, L. Marti, et al. Search for nucleon decay into charged antilepton plus meson in 0.316 megaton $\cdot$ years exposure of the super-kamiokande water cherenkov detector. *Physical Review D*, 96(1):012003, 2017.

[10] A. Abeysekara, S. Archambault, A. Archer, W. Benbow, R. Bird, R. Brose, M. Buchovecky, J. Buckley, V. Bugaev, M. Cerruti, et al. Discovery of very-high-energy emission from rgb j2243+ 203 and derivation of its redshift upper limit. *The Astrophysical Journal Supplement Series*, 233(1):7, 2017.

[11] A. Abramowski, F. Acero, F. Aharonian, A. Akhperjanian, G. Anton, U. B. De Almeida, A. Bazer-Bachi, Y. Becherini, B. Behera, W. Benbow, et al. Vhe $\gamma$-ray emission of pks 2155–304: spectral and temporal variability. *Astronomy & Astrophysics*, 520:A83, 2010.

[12] V. Acciari, E. Aliu, T. Arlen, T. Aune, M. Bautista, M. Beilicke, W. Benbow, S. Bradbury, J. Buckley, V. Bugaev, et al. Observation of extended very high energy emission from the supernova remnant ic 443 with veritas. *The Astrophysical Journal*, 698(2):L133, 2009.

[13] V. Acciari, E. Aliu, T. Arlen, M. Beilicke, W. Benbow, S. Bradbury, J. Buckley, V. Bugaev, Y. Butt, K. Byrum, et al. Veritas observations of the bl lac object 1es 1218+ 304. *The Astrophysical Journal*, 695(2):1370, 2009.

[14] V. A. Acciari, S. Ansoldi, L. Antonelli, A. A. Engels, K. Asano, D. Baack, A. Babić, B. Banerjee, U. B. de Almeida, J. Barrio, et al. New hard-tev extreme blazars detected with the magic telescopes. *The Astrophysical Journal Supplement Series*, 247(1):16, 2020.

[15] F. Acero, F. Aharonian, A. Akhperjanian, G. Anton, U. B. De Almeida, A. Bazer-Bachi, Y. Becherini, B. Behera, W. Benbow, K. Bernlöhr, et al. Pks 2005-489 at vhe: four years of monitoring with hess and simultaneous multi-wavelength observations. *Astronomy & Astrophysics*, 511:A52, 2010.

[16] F. Aharonian, A. Akhperjanian, G. Anton, U. B. De Almeida, A. Bazer-Bachi, Y. Becherini, B. Behera, W. Benbow, K. Bernlöhr, A. Bochow, et al. Discovery of vhe $\gamma$-rays from the bl lacertae object pks 0548–322. *Astronomy & Astrophysics*, 521:A69, 2010.

[17] F. Aharonian, A. Akhperjanian, A. Bazer-Bachi, M. Beilicke, W. Benbow, D. Berge, K. Bernlöhr, C. Boisson, O. Bolz, V. Borrel, et al. Discovery of very high energy $\gamma$-ray emission from the bl lacertae object h 2356-309 with the hess cherenkov telescopes. *Astronomy & Astrophysics*, 455(2):461–466, 2006.

[18] F. Aharonian, A. Akhperjanian, U. B. De Almeida, A. Bazer-Bachi, B. Behera, M. Beilicke, W. Benbow, K. Bernlöhr, C. Boisson, O. Bolz, et al. Discovery of vhe $\gamma$-rays from the distant bl lacertae 1es 0347-121. *Astronomy & Astrophysics*, 473(3):L25–L28, 2007.

[19] F. Aharonian, A. Akhperjanian, U. B. De Almeida, A. Bazer-Bachi, B. Behera, M. Beilicke, W. Benbow, K. Bernlöhr, C. Boisson, V. Borrel, et al. Discovery of vhe $\gamma$-rays from the high-frequency-peaked bl lacertae object rgb j0152+ 017. *Astronomy & Astrophysics*, 481(3):L103–L107, 2008.

[20] M. Ahnen, S. Ansoldi, L. Antonelli, P. Antoranz, A. Babic, B. Banerjee, P. Bangale, U. B. De Almeida, J. Barrio, J. B. González, et al. Long-term multi-wavelength variability and correlation study of markarian 421 from 2007 to 2009. *Astronomy & Astrophysics*, 593:A91, 2016.

[21] A. Albert, M. André, M. Anghinolfi, G. Anton, M. Ardid, J.-J. Aubert, T. Avgitas, B. Baret, J. Barrios-Martí, S. Basa, et al. First all-flavor neutrino point-like source search with the antares neutrino telescope. *Physical Review D*, 96(8):082001, 2017.

[22] E. Aliu, S. Archambault, T. Arlen, T. Aune, M. Beilicke, W. Benbow, R. Bird, A. Bouvier, J. Buckley, V. Bugaev, et al. Long term observations of b2 1215+ 30 with veritas. *The Astrophysical Journal*, 779(2):92, 2013.

[23] S. Archambault, T. Arlen, T. Aune, B. Behera, M. Beilicke, W. Benbow, R. Bird, A. Bouvier, J. Buckley, V. Bugaev, et al. Discovery of a new tev gamma-ray source: Ver j0521+ 211. *The Astrophysical Journal*, 776(2):69, 2013.

[24] S. Archambault, T. Aune, B. Behera, M. Beilicke, W. Benbow, K. Berger, R. Bird, J. Biteau, V. Bugaev, K. Byrum, et al. Deep broadband observations of the distant gamma-ray blazar pks 1424+ 240. *The Astrophysical Journal Letters*, 785(1):L16, 2014.

[25] Y. Ashie, J. Hosaka, K. Ishihara, Y. Itow, J. Kameda, Y. Koshio, A. Minamino, C. Mitsuda, M. Miura, S. Moriyama, et al. Measurement of atmospheric neutrino oscillation parameters by super-kamiokande i. *Physical Review D*, 71(11):112005, 2005.

[26] G. Barr, T. Gaisser, P. Lipari, S. Robbins, and T. Stanev. Three-dimensional calculation of atmospheric neutrinos. *Physical Review D*, 70(2):023006, 2004.

[27] G. Battistoni, A. Ferrari, T. Montaruli, and P. Sala. The fluka atmospheric neutrino flux calculation. *Astroparticle Physics*, 19(2):269–290, 2003.

[28] P. Blasi, R. I. Epstein, and A. V. Olinto. Ultra-high-energy cosmic rays from young neutron star winds. *The Astrophysical Journal*, 533(2):L123, 2000.

[29] J. Braun, M. Baker, J. Dumm, C. Finley, A. Karle, and T. Montaruli. Time-dependent point source search methods in high energy neutrino astronomy. *Astroparticle Physics*, 33(3):175–181, 2010.

[30] I. Collaboration, M. Aartsen, M. Ackermann, J. Adams, J. A. Aguilar, M. Ahlers, M. Ahrens, I. Al Samarai, D. Altmann, K. Andeen, et al. Neutrino emission from the direction of the blazar txs 0506+ 056 prior to the icecube-170922a alert. *Science*, 361(6398):147–151, 2018.

[31] I. Collaboration, Fermi-LAT, MAGIC, AGILE, ASAS-SN, HAWC, HESS, INTEGRAL, Kanata, Kiso, et al. Multimessenger observations of a flaring blazar coincident with high-energy neutrino icecube-170922a. *Science*, 361(6398):eaat1378, 2018.

[32] S. Desai. *High energy neutrino astrophysics with Super-Kamiokande*. Boston University, 2004.

[33] P. Diamond and M. Malkov. Dynamics of mesoscale magnetic field in diffusive shock acceleration. *The Astrophysical Journal*, 654(1):252, 2007.

[34] E. Fermi. On the origin of the cosmic radiation. *Physical review*, 75(8):1169, 1949.

[35] S. Fukuda, Y. Fukuda, T. Hayakawa, E. Ichihara, M. Ishitsuka, Y. Itow, T. Kajita, J. Kameda, K. Kaneyuki, S. Kasuga, et al. The super-kamiokande detector. *Nuclear Instruments and Methods in Physics Research Section A: Accelerators, Spectrometers, Detectors and Associated Equipment*, 501(2-3):418–462, 2003.

[36] M. Glück, E. Reya, and A. Vogt. Dynamical parton distributions revisited. *The European Physical Journal C-Particles and Fields*, 5(3):461–470, 1998.

[37] K. Greisen. End to the cosmic-ray spectrum? *Physical Review Letters*, 16(17):748, 1966.

[38] P. D. Group et al. Review of particle physics. *Chinese Physics C*, 40(10):100001, 2016.

[39] Y. Hayato. A neutrino interaction simulation program library neut. *Acta Physica Polonica B*, 40(9), 2009.

[40] A. Hillas, C. Akerlof, S. Biller, J. Buckley, D. Carter-Lewis, M. Catanese, M. Cawley, D. Fegan, J. Finley, J. Gaidos, et al. The spectrum of tev gamma rays from the crab nebula. *The Astrophysical Journal*, 503(2):744, 1998.

[41] M. Honda, T. Kajita, K. Kasahara, and S. Midorikawa. Calculation of the flux of atmospheric neutrinos. *Physical Review D*, 52(9):4985, 1995.

[42] M. Honda, T. Kajita, K. Kasahara, and S. Midorikawa. Improvement of low energy atmospheric neutrino flux calculation using the jam nuclear interaction model. *Physical Review D*, 83(12):123001, 2011.

[43] G. Illuminati, J. Aublin, and S. Navas. Searches for point-like sources of cosmic neutrinos with 11 years of antares data. In *36th International Cosmic Ray Conference (ICRC2019)*, volume 36, page 920, 2019.

[44] Y. Itow, T. Kajita, K. Kaneyuki, M. Shiozawa, Y. Totsuka, Y. Hayato, T. Ishida, T. Ishii, T. Kobayashi, T. Maruyama, et al. The jhf-kamioka neutrino project. *arXiv preprint hep-ex/0106019*, 2001.

[45] R. Jaffe and C. L. Smith. Deep-inelastic scattering, the subtraction of divergent sum rules, and chiral-symmetry breaking in the gluon model. *Physical Review D*, 7(8):2506, 1973.

[46] J. Kameda. *Detailed studies of neutrino oscillations with atmospheric neutrinos of wide energy range from 100 MeV to 1000 GeV in Super-Kamiokande*. PhD thesis, 2002.

[47] B. Louis, V. Sandberg, G. Garvey, H. White, G. Mills, and R. Tayloe. The evidence for oscillations. *Los Alamos Sci*, 25:16, 1997.

[48] P. F. Menéndez. *Neutrino Physics in Present and Future Kamioka Water-Čerenkov Detectors with Neutron Tagging*. Springer, 2018.

[49] P. Meszaros. Gamma-ray bursts. *Reports on Progress in Physics*, 69(8):2259, 2006.

[50] M. Nakahata, K. Arisaka, T. Kajita, M. Koshiba, Y. Oyama, A. Suzuki, M. Takita, Y. Totsuka, T. Kifune, T. Suda, N. Sato, K. Takahashi, and K. Miyano. Atmospheric neutrino background and pion nuclear effect for kamioka nucleon decay experiment. *Journal of the Physical Society of Japan*, 55(11):3786–3805, 1986.

[51] J. H. NASA, ESA and A. L. A. S. University). Messier 1 (the crab nebula). https://www.nasa.gov/feature/goddard/2017/messier-1-the-crab-nebula, 2021.

[52] H. Nishino, K. Awai, Y. Hayato, S. Nakayama, K. Okumura, M. Shiozawa, A. Takeda, K. Ishikawa, A. Minegishi, and Y. Arai. High-speed charge-to-time converter asic for the super-kamiokande detector. *Nuclear instruments and methods in physics research section a: accelerators, spectrometers, detectors and associated equipment*, 610(3):710–717, 2009.

[53] A. Panov. Electrons and positrons in cosmic rays. In *Journal of Physics: Conference Series*, volume 409, page 012004. IOP Publishing, 2013.

[54] D. Rein and L. M. Sehgal. Neutrino-excitation of baryon resonances and single pion production. *Annals of Physics*, 133(1):79–153, 1981.

[55] C. Saji. *Study of upward-going muons in Super-Kamiokande*. PhD thesis, Niigata University, 2002.

[56] R. Smith and E. J. Moniz. Neutrino reactions on nuclear targets. *Nuclear Physics B*, 43:605–622, 1972.

[57] F. W. Stecker, C. Done, M. H. Salamon, and P. Sommers. Erratum: ‘ ‘high-energy neutrinos from active galactic nuclei’ ’ [phys. rev. lett. 66, 2697 (1991)]. *Physical Review Letters*, 69(18):2738, 1992.

[58] E. Thrane, K. Abe, Y. Hayato, T. Iida, M. Ikeda, J. Kameda, K. Kobayashi, Y. Koshio, M. Miura, S. Moriyama, et al. Search for astrophysical neutrino point sources at super-kamiokande. *The Astrophysical Journal*, 704(1):503, 2009.

[59] C. M. Urry and P. Padovani. Unified schemes for radio-loud active galactic nuclei. *Publications of the Astronomical Society of the Pacific*, 107(715):803, 1995.

[60] S. P. Wakely and D. Horan. Tevcat: an online catalog for very high energy gamma-ray astronomy. In *International Cosmic Ray Conference*, volume 3, pages 1341–1344, 2008.

[61] E. Waxman. Cosmological gamma-ray bursts and the highest energy cosmic rays. *Physical Review Letters*, 75(3):386, 1995.

[62] R. J. Wilkes. Results on neutrino oscillations from super-kamiokande. *Advances in Space Research*, 26(11):1813–1822, 2000.

[63] G. T. Zatsepin and V. A. Kuz'min. Upper limit of the spectrum of cosmic rays. *Soviet Journal of Experimental and Theoretical Physics Letters*, 4:78, 1966.

[64] C. Zeitnitz and T. Gabriel. The geant-calor interface and benchmark calculations of zeus test calorimeters. *Nuclear Instruments and Methods in Physics Research Section A: Accelerators, Spectrometers, Detectors and Associated Equipment*, 349(1):106–111, 1994.